Combustion Theory and Modelling

Vol. 00, No. 00, Month 200x, 1–48

Joint-scalar transported PDF modelling of soot in a turbulent non-premixed natural gas flame

Marcus Andreas Schiener[a] and Rune Peter Lindstedt[a]*

[a]*Department of Mechanical Engineering, Imperial College, Exhibition Road, London SW7 2AZ, UK*

(*Received 00 Month 200x; final version received 00 Month 200x*)

The focus of the present work is on the prediction of soot in the turbulent Delft III / Adelaide natural gas flame at a Reynolds number of 9,700. A parabolic flow solver with the SSG Reynolds stress transport model for turbulence is coupled to a joint-scalar transported PDF approach allowing exact treatment of the interactions of turbulence with the solid and gas phase chemistries. Scalar mixing is treated via the modified Curl's coalescence/dispersion model and two different closures for the scalar dissipation rate are explored. The gas phase chemistry is represented by a systematically reduced mechanism featuring 144 reactions, 15 solved and 14 steady-state species. The dynamics of soot particles, including coagulation and aggregation in the coalescent and fractal aggregate limits, is treated either via a simplified two-equation model or via the method of moments with interpolative closure. The inclusion of soot surface reactions based on a second ring PAH analogy is also investigated. Soot oxidation via O, OH and O_2 is taken into account and the sensitivity to the applied rates investigated. An updated acetylene based soot nucleation rate is formulated based on consistency with detailed chemistry up to pyrene and combined with a sectional model to compute soot particle size distributions in the NIST well-stirred/plug flow reactor configuration. The derived rate is subsequently used in turbulent flame calculations and subjected to a sensitivity analysis. Radiative emission from soot and gas phase species is accounted for using the RADCAL method and by the inclusion of enthalpy as a solved scalar. Computed soot levels reproduce experimental data comparatively well and approximately match absolute values. The axial location of peak soot in the Delft III / Adelaide flame is consistent with previous LES simulations and possible causes for the discrepancy with experimental data analysed.

Keywords: Soot; Surface-chemistry effects; Non-premixed turbulent flames

*Corresponding author. Email: p.lindstedt@imperial.ac.uk

ISSN: 1364-7830 print/ISSN 1741-3559 online

DOI: 10.1080/13647830.YYYY.xxxxxx

http://www.tandfonline.com

Nomenclature

Latin Symbols

A_G, A_O	Soot growth and oxidation terms for method of moments
A_p	Soot surface area in m^2/particle
A_s	Soot surface area in m^2/m^3-mixture
a	Strain rate
$a_{P,i}$	Planck mean absorption coefficient of species i
b_{ij}	Anisotropy tensor
C	RADCAL model constant
C_a	Van der Waals enhancement factor
C_1, C_1^*, C_2, C_3,	Reynolds stress closure constants (see Table 2)
C_3^*, C_4, C_5, C_S	Reynolds stress closure constants (see Table 2)
$C_{S\varepsilon}$, $C_{\varepsilon 1}$, $C_{\varepsilon 2}$	Dissipation rate equation constants
C_ϕ, C_ϕ^*	Dissipation rate closure constants
C_i	Cunningham slip correction factor of size class i
C_{min}	Minimum number of carbon atoms
D_f	Fractal dimension of soot aggregates
d_c, $d_{c,i}$	Fractal aggregate diameter
d_i	Particle diameter for size class i
d_p	Mean particle diameter
$d_{p,min}$	Incipient particle diameter
d_{prim}	Diameter of primary particles (largest spherical particles)
f	Mixture fraction
$\widetilde{f_{\underline{\phi}}}$	Density-weighted PDF
f_{LFL}, f_{RFL}	Mixture fraction at lean and rich flammability limits
f_s	Geometric spacing factor for soot sections
f_{st}	Stoichiometric mixture fraction
f_v	Soot volume fraction
$f_l^{(x,y)}$	Grid function
H	Enthalpy
II	Anisotropic tensor invariant
$J_{i,a}$	Molecular diffusion flux vector
K_c, $K_c{}'$, K_f	Continuum and free molecular regime coagulation constants
k	Turbulence kinetic energy

k_B	Boltzmann constant
k_i^f	Forward rate constant for reaction i
$k_G(T)$, k_G	Soot growth reaction rate constant (see Table 5)
k_N, $k_N{}'$, $k_{N,i}$	Soot nucleation reaction rate constants (see Table 4)
$k_{\mathrm{OH},i}$, $k_{\mathrm{O},i}$, $k_{\mathrm{O}_2,i}$	Soot oxidation reaction rate constants (see Table 5)
k_i^r	Reverse rate constant for reaction i
$M_0, \ldots, M_r$	Moments of the soot particle size distribution function
M_S	Molar mass of soot
m_A	Aggregate mass
m_i	Mass per particle in section i
$m_{M,i}$	Mass per particle in section i in number of carbon atoms
m_{prim}	Mass of primary particles (largest spherical particles)
N_A	Avogadro's number
N_{bin}	Number of soot sections
N_p	Number of primary particles per soot aggregate
N_s	Soot particle number density in (particles/kg-mixture)
N_i	Number concentration of particles in section i
P_{kk}	Reynolds stress production term
$P_0, \ldots, P_r$	Moments of the size distribution of primary particles per aggregate
p_i	Partial pressure of species i
Q_{RAD}	Volumetric radiative heat loss rate
$R_0, \ldots, R_r$	Coagulation/aggregation terms for method of moments
R_G, $R_{G,i}$	Soot growth source terms
R_N, $R_N{}'$, $R_{N,i}$	Soot nucleation source terms
R_O, $R_{O,i}$	Soot oxidation source terms
$R_{C/A}$, $R_{C/A,i}$	Coagulation/aggregation source terms
S_{ij}	Mean strain tensor
S_α	Mean reaction rate of species α
T, T_b	Temperature, background temperature
T_{WSR}	Temperature in the well-stirred reactor
t	Time
$\widetilde{U}$	Favre mean axial velocity
u_i	Velocity vector
u_L	Laminar burning velocity
$\widetilde{u_i'' u_j''}$	Reynolds stress tensor
u'', v''	RMS of axial and radial velocity
u_η	Kolmogorov velocity scale

v_i	Volume per particle in section i
W_{ij}	Mean vorticity tensor
$\underline{\boldsymbol{x}}$, x_i	Cartesian coordinate vector
x	Axial coordinate in axisymmetric system
$\underline{\boldsymbol{Y}}$, Y_i	Species mass fractions
Y_s	Soot mass fraction
y	Radial coordinate in axisymmetric system

Greek Symbols

α_s	Soot surface reactivity parameter
$\beta_{j,k}$, β	Particle collision rate
δ	Jet half-width
δ_{ij}	Kronecker delta
ε	Turbulent kinetic energy dissipation rate
$\eta_{i,j,k}$	Coagulation mass distribution coefficient
λ	Gas mean free path
μ_L	Laminar dynamic viscosity
μ_r	Normalised moments M_r/M_0
μ_t	Turbulent eddy viscosity
ν	Kinematic viscosity
π_r	Normalised moments P_r/P_0
ρ, $\bar{\rho}$	Density, mean density
ρ_s	Density of soot
ρ_u	Density of unburnt reactants
σ_t	Prandtl number
σ_{SB}	Stefan-Boltzmann constant
τ_T^{-1}	Turbulence time scale
τ_ϕ^{-1}	Scalar mixing time scale
Φ	Equivalence ratio
$\underline{\boldsymbol{\phi}}$, ϕ_α	Scalar random variable
χs	PAH analogy model term
χ_{s-h}	Number of active sites per unit area on the soot surface
$\underline{\boldsymbol{\psi}}$, ψ_α	Scalar sample space of $\underline{\boldsymbol{\phi}}$, ϕ_α
ω	Normalised stream function coordinate

Subscripts

α	Scalar field index
$a2$	Secondary air co-flow

f	Fuel jet

Superscripts

$\sim$	Density-weighted average
$''$	Favre fluctuation
A	Aggregation
C	Cogulation
c	Continuum regime of coagulation/aggregation
f	Free molecular regime of coagulation/aggregation
t	Transition regime of coagulation/aggregation

Abbreviations

Kn	Knudsen number
Re	Reynolds number

1. Introduction

The improvement of soot predictions in turbulent flames remains important for the reduction of particulate emissions in practical applications. Historically, most soot models have relied on numerical solutions with different degrees of simplification of some form of the transport equation for the particle number density function (NDF), e.g. a population balance equation (PBE), evolved from Smoluchowski's master equation describing particle coagulation [1]. One approach to solving the PBE is the discretisation along an internal variable of the NDF into sections. The internal variable used is commonly describing the particle size only, e.g. via volume or mass [2], although other internal variables such as surface area or chemical composition may be taken into account [3]. The approach renders the solution of the PBE numerically feasible and the development of such methods and their application to soot modelling has been pursued by Smooke et al. [4] amongst others. Kumar and Ramkrishna [5] developed a fixed sectional model preserving mass and number density, offering both numerical accuracy and speed. Bhatt and Lindstedt [6] and Lindstedt and Waldheim [7] developed the approach to model soot in a well-stirred/plug

flow reactor configuration [8, 9] and for premixed laminar flames [10–12]. The stability of surface growth and oxidation terms was addressed via the 'two-point' and 'three-point' methods by Park and Rogak [13].

Instead of attempting to solve an approximation of the NDF directly, moment methods [14] transport a finite set of moments [3], making such approaches computationally less expensive. The method of moments with interpolative closure (MOMIC) [15] is using an interpolation approach based on the transported moments for closure of the moment equation. Quadrature based moment approaches reconstruct the NDF to solve the closure problem and a number of strategies for discrete (quadrature [16], direct quadrature [17], hybrid [18] and conditional quadrature [19] methods of moments) and continuous (extended conditional quadrature method of moments [20]) reconstruction have been developed. In two-equation type soot models [21, 22], equations for soot mass and particle number density are solved. The method is functionally equivalent to a moment approach solving for the zeroeth and first moments of the particle size distribution function only.

A particular issue with soot formation and oxidation in turbulent flames is that the chemistry tends to be slow compared to the majority of gas phase reactions. Accordingly, the need arises to solve additional transport equations for soot related properties (e.g. soot mass and number density) with, for example, soot treated as a perturbation upon the gas phase chemistry combined with a presumed PDF approach [23, 24]. Such approaches fail when a significant proportion of the available carbon is converted to soot and also present problems due to the radiative heat loss effects typically associated with soot formation. Transported probability density function (PDF) methods offer the principal advantage of treating the highly non-linear chemical source terms occurring in turbulent combustion modelling without approximation [25], can be extended to Large Eddy Simulations (LES) [26], provide a direct coupling between gas and soot chemistries and can readily include enthalpy as part of the solved scalar space [27, 28]. In the current work, a transported PDF

approach closed at joint-scalar level is adopted requiring closure approximations only for turbulent transport in physical space and molecular mixing in composition space.

The Delft III / Adelaide flame ("Delft flame") [29] is a piloted turbulent non-premixed flame burning natural gas, and has been designated a target flame of the International Sooting Flame (ISF) workshop [30] series. It remains relevant for the validation of soot models under turbulent conditions particularly due to the use of a methane-based fuel and the extensive measurements performed. The experimental dataset available for this flame includes laser-Doppler anemometry (LDA) velocity measurements reported by Stroomer et al. [31], data on mean and variance of scalars, the PDF of mixture fraction and joint measurements of mixture fraction and scalars by Nooren et al. [32, 33] using Raman-Rayleigh-LIF (RRL) and laser-induced incandescence (LII) soot measurements by Qamar et al. [34]. Calculations of soot statistics in this flame have been carried out by Mueller and Pitsch [35] and Donde et al. [36] using LES with a flamelet / progress variable approach and a hybrid method of moments model [18] for particle dynamics. Good agreement was reported for velocity and scalar fields, while the location of the peak mean soot volume fraction was predicted 30–40 nozzle diameters upstream of the experimental location with maximum soot levels overpredicted by factors of 3–5.5 [35] and 6.5 [36]. The disagreement was attributed to uncertainties in the sub-filter dissipation rate model and the PAH chemistry, with the computed early soot onset attributed to the latter. Further computational studies investigating the non-sooting aspects of the Delft flame have been carried out [37–42]. Merci et al. [38, 39] used conserved scalar presumed PDF and joint-scalar transported PDF approaches. For the latter, the applied pilot model was found to have a strong influence on the flow field close to the nozzle exit, while the effect on the global flame shape was small [38]. The performance of three different micromixing models was also assessed [39]. Global flame extinction was observed with the interaction by exchange with the mean (IEM) model and local extinction was found to be underpredicted with the

Euclidean Minimum Spanning Tree (EMST) model. The Curl's coalescence/dispersion model was used to investigate the sensitivity to (i) the thermal power introduced by the pilot and (ii) to the model constant C_ϕ affecting the mixing frequency. It was found that either increasing the pilot power by 50 % or the value of C_ϕ to 3.0 was required for flame attachment to the burner. Ayache and Mastorakos [42] modelled the flame using LES with a conditional moment closure (CMC) sub-grid model and successfully captured local extinction and re-ignition close to the burner.

The current investigation extends past efforts to model the Delft flame using a joint-scalar transported PDF modelling approach [28] with soot particle dynamics treated via two-equation (e.g. [21, 22]) and method of moment with interpolative closure (MOMIC) [15] based models. The approach, in principle, eliminates uncertainties associated with the influence of turbulence-chemistry interactions. The sensitivity to soot nucleation rates is assessed by comparing computed soot particle size distributions (PSDs) in the NIST combined well-stirred (WSR) and plug flow (PFR) reactor configuration of Manzello et al. [8, 9]. Updated rates that are consistent with both the experimental data and pyrene nucleation rates, obtained using detailed chemistry [7], are derived and subsequently applied in computations of the Delft flame. A sensitivity analysis is performed to elucidate the impact of nucleation rate uncertainties on the location of the peak soot concentration and possible causes analysed. Soot oxidation rates are also updated with recent recommendations and the impact assessed in both configurations.

2. Computational Model

2.1 *General Model*

The computational approach applied to the turbulent Delft III / Adelaide natural gas flame is based on that of Lindstedt and Louloudi [28, 43] and features a two-dimensional im-

plicit parabolic flow solver, based on the x–ω transformation [44], coupled with a Lagrangian particle implementation for the transported PDF method. The governing equations including the transport equation for the joint-scalar PDF and the Reynolds stress turbulence closure are shown in Table 2. The velocity field is obtained via the Speziale, Sarkar and Gatski (SSG) second order closure [45] and the generalized gradient diffusion assumption [46]. The scalar mixing term in the transported PDF equation is modelled using the modified Curl's model of Janicka et al. [47] with standard and extended closures for the scalar dissipation rate as discussed below. The gas phase chemistry is that previously used by Lindstedt and Louloudi [28, 43] and features 144 reactions, 15 solved (H, O, OH, HO_2, H_2O, H_2, O_2, CO, CO_2, CH_3, CH_4, C_2H_2, C_2H_4, C_2H_6, and N_2) and 14 steady-state species (C, CH, $^1CH_2$, $^3CH_2$, CHO, CH_2OH, CH_3O, C_2, C_2H, C_2H_3, C_2H_5, C_2HO, C_2H_2O, and CH_2O, including methylene in singlet and triplet spin states). Soot is included using two alternative methods: The solution of two additional equations [21, 22, 28] for soot mass (Y_s) and number density (N_s), and the alternative treatment of soot particle dynamics via the method of moments with interpolative closure (MOMIC) [15]. For the two-equation model the joint-scalar PDF may be expressed as $\widetilde{f}_{\underline{\phi}} = (\underline{\psi}; \underline{x}, t)$, where $\underline{\psi}$ is the sample space of the random vector $\underline{\phi} = (\underline{\mathbf{Y}}, H, Y_s, N_s, f)$, whereas for the latter case the first four moments ($M_0 - M_3$) of the soot particle size distribution function (PSDF) and the first two moments ($P_1 - P_2$) of the size distribution of primary soot particles per aggregate are included, such that the vector becomes $\underline{\phi} = (\underline{\mathbf{Y}}, H, M_0, M_1, M_2, M_3, P_1, P_2, f)$. The mass fractions of species are denoted $\underline{\mathbf{Y}}$ and enthalpy (H). The mixture fraction (f) is also included for post-processing purposes only. Radiative heat losses from gas phase species H_2O, CO, CO_2 and CH_4 and soot are accounted for by means of an optically thin model [48, 49],

$$Q_{RAD} = 4\sigma_{SB} \times \left(\sum_{i=1}^{K} p_i a_{P,i} \left(T^4 - T_b^4 \right) \right) + 4\sigma_{SB} C f_v \left(T^5 - T_b^5 \right) \tag{1}$$

where σ_{SB} is the Stefan–Boltzmann constant (5.669×10^{18} W m^{-2} K^{-4}), p_i is the partial pressure of species i in atmospheres, $a_{P,i}$ the Planck mean absorption coefficient of species i in [m^{-1} atm^{-1}], T the local temperature, $T_b = 295$ K is the background temperature, $C = 1.307 \times 10^3$ m^{-1} K^{-1} [43], and f_v is the local soot volume fraction.

2.2 *Soot Models*

Analytical solutions to Smoluchowki's master equation [1] for the dynamics of soot particles do not generally exists and the direct numerical integration is prohibitively expensive [14, 50, 51]. The use of moment based [15] or sectional [6] models for the determination of the particle size distribution is comparatively affordable. To elucidate the role of the applied soot nucleation and oxidation rates, predictions of soot particle size distributions in the combined WSR/PFR reactor configuration of Manzello et al. [8, 9] are presented below. In particular, the calculations provide an alternative evaluation of the impact of simplified soot nucleation rate expressions.

2.2.1 Sectional Model

The soot mass and number density preserving fixed sectional approach of Bhatt and Lindstedt [6], based on that by Kumar and Ramkrishna [5], is combined with the detailed chemical mechanism by Lindstedt and Waldheim [7] featuring 357 species up to pyrene and 1789 reactions. The sectional bins are distributed geometrically using a a spacing factor f_s (= 1.5) as

$$m_{i+1} = f_s m_i. \tag{2}$$

The approach is computationally efficient with soot mass assigned as the representative

size variable. For a number of N_{bin} representative sizes, the corresponding population balance equations for coagulation/aggregation are given by,

$$\frac{\mathrm{d}N_i}{\mathrm{d}t} = \sum_{\substack{k\le j\le i \\ j,k \\ m_{i-1}\le(m_j+m_k)\le m_{i+1}}} \left(1-\frac{\delta_{jk}}{2}\right)\eta_{i,j,k}\beta_{j,k}N_jN_k - N_i\sum_{k=1}^{N_{\text{Bin}}}\beta_{i,k}N_k \tag{3}$$

where N_i is the number concentration of the ith size class, $\beta_{j,k}$ the rate of collision of particles of size class j with class k and δ_{jk} is the Kronecker delta. Newly formed particles are assigned to two adjacent bins, conserving any two general properties if new particles do not match any of the representative sizes exactly. The parameter $\eta_{i,j,k}$ is the fraction of a newly created particles assigned to size class i when two particles of classes j and k collide, hence assigning new particles to two adjacent bins as

$$\eta_{i,j,k} = \begin{cases} \frac{m_{i+1}-(m_j+m_k)}{m_{i+1}-m_i}, & m_i \le (m_j+m_k) \le m_{i+1} \\ \frac{m_{i-1}-(m_j+m_k)}{m_{i-1}-m_i}, & m_{i-1} \le (m_j+m_k) \le m_i. \end{cases} \tag{4}$$

Coagulation and aggregation of particles are considered in the limits of the free molecular regime with a Knudsen (Kn) number $\gg 1$ and the continuum regime $\mathrm{Kn} \ll 1$, as well as the transition regime [51]. The transition regime is here assumed to be within the boundaries $0.1 \le \mathrm{Kn} \le 10$, with values of the Knudsen number above or below corresponding to the limit cases. The Knudsen number $\mathrm{Kn} = 2\lambda/d_i$ is evaluated in terms of the gas mean free path λ and the particle diameter d_i. The rate constants for spherical particles in the three regimes are then given by Eqs. (5)–(7) [15, 52], where the collision frequency in the transition regime is approximated by the harmonic average of the limiting cases.

$$\beta_{i,j}^{C,f} = C_a\left(\frac{3}{4\pi}\right)^{1/6}\left(\frac{6k_BT}{\rho_s}\right)^{1/2}\left(\frac{1}{v_i}+\frac{1}{v_j}\right)^{1/2}\left(v_i^{1/3}+v_j^{1/3}\right)^2 \tag{5}$$

$$\beta_{i,j}^{C,c} = \frac{2k_BT}{3\mu_L}\left(\frac{C_i}{v_i^{1/3}}+\frac{C_j}{v_j^{1/3}}\right)\left(v_i^{1/3}+v_j^{1/3}\right) \tag{6}$$

$$\beta_{i,j}^{t} = \frac{\beta_{i,j}^{f}\beta_{i,j}^{c}}{\beta_{i,j}^{f} + \beta_{i,j}^{c}} \tag{7}$$

The superscript C denotes coagulation into spherical particles, f, c and t the free, continuum and transition regimes, respectively, v_i is the volume of a particle of size class i and d_i its diameter, $\rho_s = 2000$ kg/m^3 is the density of soot, $k_B = 1.38 \cdot 10^{-23}$ J/K the Boltzmann constant, T the temperature, μ_L the laminar dynamic viscosity of the fluid, C_i the Cunningham slip correction factor given by Eq. (8) [52] and $C_a = 3$ [7] is the van der Waals enhancement factor.

$$C_i = 1 + 1.257\ \mathrm{Kn} \tag{8}$$

Aggregation (or agglomeration) is characterised by the creation of chain-like structures after collision of similarly sized primary particles, replacing coalescent growth in the limit of large mean particle diameters. There exists no satisfactory model describing the transition from coalescent growth to aggregation, and in the current work the mean particle diameter at which aggregation replaces coagulation is set to 27.5 nm following Kazakov and Frenklach [51] who used values in the range 25 – 30 nm. The diameter of the fractal aggregates follows from Eq. (9) based on the primary particle diameter (d_{prim}) and the number of primary particles per aggregate (N_p) with a fractal dimension $D_f = 1.8$ [53].

$$d_c = d_{prim} {N_p}^{1/D_f} \tag{9}$$

Assuming identical mobility and collision diameters, aggregation rates in the two limiting regimes are taken as [54],

$$\beta_{i,j}^{A,f} = C_a \left(\frac{\pi k_B T}{2}\right)^{1/2} \left(\frac{1}{m_i} + \frac{1}{m_j}\right)^{1/2} \left(d_{c,i} + d_{c,j}\right)^2 \tag{10}$$

$$\beta_{i,j}^{A,c} = \frac{2k_B T}{3\mu_L} \left(\frac{C_i}{d_{c,i}} + \frac{C_j}{d_{c,j}}\right) \left(d_{c,i} + d_{c,j}\right) \tag{11}$$

where the superscript A denotes aggregation involving chain-like fractal aggregates. Both terms are combined in the transition regime via Eq. (7).

Growth and oxidation in the sectional model are treated via the 'two-point' fixed sectional approach by Park and Rogak [13]. The corresponding reaction rates and the treatment of soot nucleation are discussed in Section 2.3. The soot mass and particle number density are linked directly via the properties of the soot sections.

2.2.2 Two-Equation Model

The above approach is used to evaluate the impact of simplified soot nucleation and revised oxidation rates. However, soot PSDs for turbulent flames are scarce and in the current work simplifications for the particle dynamics are introduced while retaining the rates of reaction. In two-equation approaches to soot modelling [21, 22] a single mean particle size is adopted and the evolution of the soot particle number density is calculated by integration of Eq. (12), corresponding to the equation for the zeroeth moment of the PSDF in method of moment type approaches.

$$\frac{d[\rho N_s]}{dt} = R_N{}' - R_{C/A} \tag{12}$$

The total number density (particles/kg-mixture) is denoted by N_s (i.e. the sum of all particles across all size classes). The nucleation term ($R_N{}'$) is discussed below with coagulation/aggregation ($R_{C/A}$) defined as,

$$R_{C/A} = \frac{1}{2}\sum_{i=1}^{\infty}\sum_{j=1}^{\infty}\beta_{i,j}[\rho N_i][\rho N_j] \tag{13}$$

$$= \frac{1}{2}\beta[\rho N_s]^2 \tag{14}$$

where $[\rho N_i]$ is the number density (particles/m^3) of particles of size class i and $\beta_{i,j}$ the collision frequency with Eq. (13) simplified via Eq. (15) under the assumption of a nearly

monodisperse and sufficiently diluted system [55].

$$N_s = \sum_{i=1}^{\infty} N_i \tag{15}$$

A separate equation for the soot mass fraction (Y_s) is solved fully coupled with the gas phase. The source term for soot mass is calculated via a Newton linearisation procedure, with all soot reactions considered irreversible [56], taking into account nucleation (R_N), surface growth (R_G) and oxidation (R_O), as discussed in Sections 2.3.1–2.3.3,

$$\rho S_{Y_s} = \left[2R_N + 2R_G - R_O\right] \cdot M_s \tag{16}$$

where the molar mass of soot (M_s) is taken to be that of carbon (12.019 kg kmol^{-1}).

The equations for soot mass and number density are linked via the mean particle diameter d_p, calculated from Eq. (17) as a function of the soot mass fraction Y_s, the number density N_s and the gas (ρ) and soot (ρ_s) densities [22].

$$d_p = \left(\frac{6}{\pi}\frac{\rho}{\rho_s}\frac{Y_s}{\left[\rho N_s\right]}\right)^{1/3} \tag{17}$$

Similar to the sectional model, the collision frequency β in Eq. (14) is obtained in the limits of the free molecular and continuum regimes, and in the transition regime via Eq. (7). The superscript notation from Eqs. (5)–(7) and (10)–(11) is retained, with the subscript i,j omitted due to the assumption of a single mean particle size. Under the assumption of monodispersity, Eq. (5) can be written as

$$\begin{aligned}\beta^{C,f} &= C_a \left(\frac{3}{4\pi}\right)^{1/6} \left(\frac{6k_BT}{\rho_s}\right)^{1/2} \left(\frac{2}{v_i}\right)^{1/2} \left(2v_i^{1/3}\right)^2 \\ &= 4C_a \left(\frac{6k_BT}{\rho_s}\right)^{1/2} \left(\frac{6}{\pi}v_i\right)^{1/6}.\end{aligned} \tag{18}$$

Writing the mean particle volume as $v_i = Y_s/(\rho_s N_s)$ and assuming spherical particles, the collision frequency in the free molecular regime (Kn > 10) is obtained via Eq. (17),

$$\begin{aligned}\beta^{C,f} &= 4C_a \left(\frac{6k_BT}{\rho_s}\right)^{1/2} \left(\frac{6}{\pi}\frac{Y_s}{\rho_s N_s}\right)^{1/6} \\ &= 4C_a \left(\frac{6k_BT}{\rho_s}\right)^{1/2} {d_p}^{1/2}\end{aligned} \tag{19}$$

where the value $C_a = 9$ was retained to provide continuity with previous work [28, 43] to reproduce the measured evolution of the (mean) soot particle number density in a set of laminar diffusion flames [21, 22]. Similarly, Eq. (6) can be rewritten for a monodisperse PSD, giving the collision frequency in the continuum regime (Kn < 0.1) as

$$\begin{aligned}\beta^{C,c} &= \frac{2k_BT}{3\mu_L} \left(\frac{2C_i}{v_i^{1/3}}\right) \left(2v_i^{1/3}\right) \\ &= \frac{8k_BT}{3\mu_L} C_i \,.\end{aligned} \tag{20}$$

Likewise, rates of aggregation in the free molecular and continuum regimes can be obtained for a monodisperse system from Eqs. (10)–(11) as

$$\begin{aligned}\beta^{A,f} &= C_a \left(\frac{\pi k_BT}{2}\right)^{1/2} \left(\frac{2}{m_A}\right)^{1/2} \left(2d_c\right)^2 \\ &= 4C_a \left(\pi k_BT\right)^{1/2} \frac{{d_c}^2}{{m_A}^{1/2}} \,,\end{aligned} \tag{21}$$

$$\begin{aligned}\beta^{A,c} &= \frac{2k_BT}{3\mu_L} \left(\frac{2C_i}{d_c}\right) \left(2d_c\right) \\ &= \frac{8k_BT}{3\mu_L} C_i \,.\end{aligned} \tag{22}$$

The diameter (d_c) of fractal aggregates is defined by Eq. (9). Primary particles (d_{prim} = 27.5 nm) are the largest spherical particles formed via coagulation. In the context of the moment methods calculations, the mass of a primary particle is directly obtained from d_{prim} by assuming a spherical shape.

$$m_{prim} = \frac{\pi}{6}\rho_s {d_{prim}}^3 \tag{23}$$

As for spherical particles, soot aggregates are represented via a mean particle size, expressed as the aggregate mass m_A (in kg/particle). It is directly deduced from the soot mass

fraction Y_s (in kg-soot/kg-mixture) and the number density N_s (in particles/kg-mixture), as shown in Eq. (24). The relation is independent of the particle shape, and also implicitly used in the calculation of the diameter of spherical particles in Eq. (17).

$$m_A = \frac{Y_s}{N_s} \tag{24}$$

The number of primary particles per aggregate N_p may then be calculated as the ratio of the aggregate and primary particle masses:

$$N_p = \frac{m_A}{m_{prim}}. \tag{25}$$

The collision rate for coagulation and aggregation in the transition regime is obtained via harmonic averaging.

2.2.3 Method of Moments with Interpolative Closure

In addition to the integration of Eq. (12), the particle dynamics in the Delft flame are also modelled via the method of moments with interpolative closure defined by Frenklach [15] and as used by Lindstedt and Louloudi [28, 43]. In this approach, Smoluchowski's equation is rewritten in terms of the r-th order moment of the PSDF defined as [50],

$$M_r = \sum_{i=1}^{\infty} m_{M,i}^r \left[\rho N_i\right] \tag{26}$$

where $m_{M,i}$ is the mass in number of carbon atoms and N_i the number density (particles/kg-mixture) of the soot particles of size class i. The resulting set of equations may then be extended to account for nucleation, oxidation and coalescence or aggregation, such that the evolution of the moments is obtained as [28, 50],

$$\begin{aligned}
\frac{dM_0}{dt} &= R_{N,0} - R_{C/A,0} \\
\frac{dM_1}{dt} &= R_{N,1} + R_{G,1} - R_{O,1} \\
\frac{dM_2}{dt} &= R_{N,2} + R_{C/A,2} + R_{G,2} - R_{O,2} \\
&\dots \\
\frac{dM_r}{dt} &= R_{N,r} + R_{C/A,r} + R_{G,r} - R_{O,r}
\end{aligned} \tag{27}$$

where the subscript N indicates nucleation, C/A coagulation and aggregation, G mass growth and O oxidation. The solution obtained for the first four moments ($M_0 - M_3$) is here used as an alternative to the two-equation model, with the terms in Eq. (27) as defined by Lindstedt and Louloudi [28, 43]. The equations for the zeroeth (M_0) and first (M_1) moments correspond, respectively, to the soot number density and soot mass equations.

As for the sectional and two-equation models described in previous sections, particle collisions are considered as coagulation of small spherical particles or as aggregation of fractal aggregates, in either the free molecular (Kn > 10) , the continuum (Kn < 0.1), or the transition regime $0.1 \leq \mathrm{Kn} \leq 10$. In the free molecular regime of coagulation, the terms $R_{C/A,r} = R_r^{C,f}$ in Eq. (27) are expressed as [14],

$$R_0^{C,f} = \frac{1}{2} K_f M_0^2 f_{1/2}^{(0,0)}, \tag{28}$$

$$R_r^{C,f} = \frac{1}{2} K_f M_0^2 \sum_{k=1}^{r-1} \binom{r}{k} f_{1/2}^{(k,r-k)} \quad \text{for} \quad r = 2, 3, \dots \tag{29}$$

with

$$K_f = C_a \left(\frac{6 k_B T}{\rho_s} \right)^{1/2} \left(\frac{3 M_s}{4 \pi \rho_s N_A} \right)^{1/6}. \tag{30}$$

The general definition of the grid function $f_l^{(x,y)}$ is given by Eq. (31), and $f_{1/2}^{(k,r-k)}$ in Eq. (29) is obtained by Lagrange quadratic interpolation as outlined by Frenklach [15] and is here included for completeness.

$$f_l^{(x,y)} = \sum_{i=1}^{\infty}\sum_{j=1}^{\infty}\left(m_{M,i}+m_{M,j}\right)^l m_{M,i}^{x-1/2} m_{M,j}^{y-1/2}\left(m_{M,i}^{1/3}+m_{M,j}^{1/3}\right)^2 N_i N_j \tag{31}$$

$$f_{1/2}^{(k,r-k)} = \left(f_0^{(k,r-k)}\right)^{3/8}\left(f_1^{(k,r-k)}\right)^{3/4}\left(f_2^{(k,r-k)}\right)^{-1/8} \tag{32}$$

Coagulation terms $R_{C/A,r} = R_r^{C,c}$ in the continuum regime also follow Franklach [15],

$$R_0^{C,c} = K_c\left[1+\mu_{1/3}\mu_{-1/3}+K_c'\left(\mu_{-1/3}+\mu_{1/3}+\mu_{-2/3}\right)\right]M_0^2 \tag{33}$$

$$\begin{aligned} R_r^{C,c} = {} & \frac{1}{2}K_c\sum_{k=1}^{r-1}\binom{r}{k}\Big[2\mu_k\mu_{r-k}+\mu_{k+1/3}\mu_{r-k-1/3} \\ & +\mu_{k-1/3}\mu_{r-k+1/3}+K_c'\big(\mu_{k-1/3}\mu_{r-k}+\mu_k\mu_{r-k-1/3} \\ & \mu_{k+1/3}\mu_{r-k-2/3}+\mu_{k-2/3}\mu_{r-k+1/3}\big)\Big]M_0^2 \quad \text{for} \quad r=2,3,\ldots \end{aligned} \tag{34}$$

with

$$K_c = \frac{2k_BT}{3\mu_L} \tag{35}$$

$$K_c' = 2.154\lambda\left(\frac{\pi\rho_s N_A}{6M_s}\right)^{1/3} \tag{36}$$

and where $\mu_r = M_r/M_0$ denotes the normalised moments. For aggregation in the free molecular regime, the terms $R_{C/A,r} = R_r^{A,f}$ are defined analogously to Eqs. (28)–(29), with a correspondingly modified grid function as shown by Kazakov and Frenklach [51].

$$R_0^{A,f} = \frac{1}{2}K_f M_0^2 f_{1/2}^{(0,0)} \tag{37}$$

$$R_r^{A,f} = \frac{1}{2}K_f M_0^2\sum_{k=1}^{r-1}\binom{r}{k}f_{1/2}^{(k,r-k)} \quad \text{for} \quad r=2,3,\ldots \tag{38}$$

$$\begin{aligned} f_l^{(x,y)} = {} & \sum_{k=0}^{l}\binom{l}{k}\Big(\left\langle m_A^{x+k+1/6}N_p^{2/D_f-2/3}\right\rangle\mu_{y+l-k-1/2} \\ & +2\left\langle m_A^{x+k-1/6}N_p^{1/D_f-1/3}\right\rangle\left\langle m_A^{y+l-k-1/6}N_p^{1/D_f-1/3}\right\rangle \\ & +\mu_{x+k-1/2}\left\langle m_A^{y+l-k+1/6}N_p^{2/D_f-2/3}\right\rangle\Big) \end{aligned} \tag{39}$$

Similarly, for aggregation in the continuum regime $R_{C/A,r} = R_r^{A,c}$, with

$$
\begin{aligned}
R_0^{A,c} = \; & K_c \Big[1 + \left\langle m_A^{1/3} N_p^{1/D_f - 1/3} \right\rangle \left\langle m_A^{-1/3} N_p^{1/3 - 1/D_f} \right\rangle \\
& + K_c{}' \Big(\left\langle m_A^{-1/3} N_p^{1/3 - 1/D_f} \right\rangle \\
& + \left\langle m_A^{1/3} N_p^{1/D_f - 1/3} \right\rangle \left\langle m_A^{-2/3} N_p^{2/D_f - 2/3} \right\rangle \Big) \Big] M_0^2 \qquad (40) \\
R_r^{A,c} = \; & \frac{1}{2} K_c \sum_{k=1}^{r-1} \binom{r}{k} \Big[2 \mu_k \mu_{r-k} \\
& + \left\langle m_A^{k+1/3} N_p^{1/D_f - 1/3} \right\rangle \left\langle m_A^{r-k-1/3} N_p^{1/3 - 1/D_f} \right\rangle \\
& + \left\langle m_A^{k-1/3} N_p^{1/3 - 1/D_f} \right\rangle \left\langle m_A^{r-k+1/3} N_p^{1/D_f - 1/3} \right\rangle \\
& + K_c{}' \Big(\left\langle m_A^{k-1/3} N_p^{1/3 - 1/D_f} \right\rangle \mu_{r-k} + \mu_k \left\langle m_A^{r-k-1/3} N_p^{1/3 - 1/D_f} \right\rangle \\
& + \left\langle m_A^{k+1/3} N_p^{1/D_f - 1/3} \right\rangle \left\langle m_A^{r-k-2/3} N_p^{2/3 - 2/D_f} \right\rangle \\
& + \left\langle m_A^{k-2/3} N_p^{2/3 - 2/D_f} \right\rangle \left\langle m_A^{r-k+1/3} N_p^{1/D_f - 1/3} \right\rangle \Big) \Big] M_0^2 \quad \text{for} \quad r = 2, 3, \ldots . \qquad (41)
\end{aligned}
$$

The terms $\left\langle m_A^r N_p^{r'} \right\rangle$ in Eqs. (39)–(41) require knowledge of the joint PDF of mass and number density, and the following approximation [51] is adopted,

$$
\left\langle m_A^r N_p^{r'} \right\rangle \approx \left\langle m_A^r \right\rangle \left\langle N_p^{r'} \right\rangle = \mu_r \pi_{r'} \qquad (42)
$$

where the normalised primary particle moments are defined by $\pi_{r'} = P_{r'}/P_0$. The fractional order moments μ_r and $\pi_{r'}$ appearing in the source terms above are computed via the whole order moments using Lagrange logarithmic interpolation [15, 43].

As in the sectional and two-equation models, the terms in the transition regime of either coagulation or aggregation are obtained via harmonic averaging of the expressions corresponding to the limit. The expression for aggregation is given below.

$$
R_r^{A,t} = \frac{R_r^{A,f} R_r^{A,c}}{R_r^{A,f} + R_r^{A,c}} \qquad (43)
$$

A separate set of equations for the moments of the size distribution of primary particles is solved, with an explicit equation for $P_0 = M_0$ omitted.

$$\begin{aligned} \frac{dP_1}{dt} &= R_{N,0}, \\ \frac{dP_r}{dt} &= R_{N,0} + H_r \quad \text{for} \quad r = 2, 3, \ldots \end{aligned} \tag{44}$$

A two-moment model for primary particles (P_1, P_2) is considered to be sufficiently accurate, following Kazakov and Frenklach [51]. The coagulation term is represented by H_r, and is computed in the different regimes similarly to Eqs. (29)–(41) [15, 43].

The treatment of the nucleation (i.e. $R_{N,r}$) is discussed in Section 2.3.1. The source terms for growth and oxidation were obtained under the assumption of spherical particles and a linear dependency on the surface area [14, 15],

$$R_{G,r} = A_G N_A \pi d_{p,min}^2 M_0 \sum_{k=0}^{r-1} \binom{r}{k} 2^{r-k} \mu_{k+2/3} \tag{45}$$

$$R_{O,r} = A_O N_A \pi d_{p,min}^2 M_0 \sum_{k=0}^{r-1} \binom{r}{k} (-2)^{r-k} \mu_{k+2/3} \tag{46}$$

where the terms A_G and A_O provide the coupling to the gas phase chemistry as discussed in Section 2.3 below. To reflect the change of particle surface area for aggregates [15], the terms are modified in the aggregation regime (e.g. [28]):

$$R_{G,r} = A_G N_A \pi d_{p,min}^2 M_0 \sum_{k=0}^{r-1} \binom{r}{k} 2^{r-k} \left\langle m_A^{k+2/3} N_p^{1/3} \right\rangle \tag{47}$$

$$R_{O,r} = A_O N_A \pi d_{p,min}^2 M_0 \sum_{k=0}^{r-1} \binom{r}{k} (-2)^{r-k} \left\langle m_A^{k+2/3} N_p^{1/3} \right\rangle \tag{48}$$

2.3 *Soot Formation and Oxidation*

2.3.1 Nucleation

The transported PDF method provides the full turbulence-chemistry interactions associated with the applied chemical mechanism. Accordingly, simplifications to the nucleation step are highly desirable as the PAH chemistry inevitably leads to a significant increase in

the size of the scalar space. Past work [21, 22, 28] has featured nucleation steps formulated as first order in the acetylene concentration via Eqs. (49)–(50),

$$C_2H_2 \longrightarrow 2\,C_{soot} + H_2 \tag{49}$$

$$R_N = k_N(T)\left[C_2H_2\right] \tag{50}$$

where C_{soot} denotes carbon atoms contributing to the soot particle mass. The reaction is assumed irreversible with a reduction in soot mass caused by oxidation and in the particle number density caused by coagulation/aggregation. Equation (49) also gives rise to the source term $R_N{}'$ in the number density equation of the two-equation model (Eq. (51)) and the terms $R_{N,r}$ in the context of the method of moments with interpolation (Eqs. (27) and (44)), where C_{min} is the number of carbon atoms in an incipient soot particle.

$$R_N{}' = 2N_A k_N{}'(T)\left[C_2H_2\right] = R_{N,r} \quad \text{for} \quad r = 0, 2, 3, \ldots \tag{51}$$

$$k_N{}'(T) = k_N(T)/C_{min} \tag{52}$$

The parameter C_{min} (= 60) can be interpreted as providing a scaling for the source term in the particle number density equation that improves consistency of predictions of both soot mass and number density within the framework of simplified models. The link to the soot mass equation is via the particle size in the growth and oxidation rate expressions.

Modelling nucleation in the absence of reliable compact reduced models for PAH molecules relies upon a correlation between PAH and C_2H_2 concentrations. Sunderland et al. [57], Lin et al. [58], and Sunderland and Faeth [59] measured soot nucleation and growth for laminar diffusion flames across a wide range of conditions and fuels and proposed nucleation rates based on a first order correlation with the acetylene concentration. Fuels considered included ethane, propane, *n*-butane, ethylene, propylene and 1,3-butadiene, and it was shown that nucleation correlates with acetylene concentration

largely independently of the fuel used [59]. Louloudi [43] and Lindstedt and Louloudi [28] modelled nucleation in the turbulent ethylene diffusion flames of Kent and Honnery [60] and Coppalle and Joyeux [61] using a reaction step previously validated in laminar non-premixed methane, ethylene, propane flames [21, 22]. The current work compares these nucleation rates with a more accurate formulation based on computed pyrene concentration using the detailed chemistry of Lindstedt and Waldheim [7]. The impact on the evolution of the PSD is assessed against the experimental data obtained by Lenhert and Manzello [9] in a WSR/PFR reactor configuration by using a sectional model [6, 7]. In sectional models, the particle number density and soot mass are intrinsically linked via the particle mass assigned to each section. The nucleation step accordingly represents both a source of soot mass and particle number density in the smallest section. For consistency, soot nucleation is treated via Eq. (53) with the incipient soot particles assigned the molecular mass and thermodynamic properties of pyrene.

$$8C_2H_2 \longrightarrow C_{16}H_{10} + 3H_2 \tag{53}$$

For a given nucleation rate, reactions Eqs. (49) and (53) yield approximately the same mass of soot per mole of C_2H_2 ($2M_C \approx M_{C_{16}H_{10}}/8$). By contrast, in the two-equation model, the reaction rate constant in the number density source term is scaled relative to that of the mass source term via $k_N{}' = k_N/C_{min}$ and the different stoichiometric coefficients in Eq. (49) and (53) are not balanced by the difference in molar mass of soot. As a result, for any given rate of reaction, the number density source term in the two-equation model yields $2/C_{min}$ moles of soot per mole of C_2H_2, whereas in the sectional model Eq. (53) gives 1/8 moles of incipient soot particles, an increase by approximately a factor of 3.75. The nucleation rates in the sectional model calculations have been scaled accordingly to ensure consistency with the two-equation and method of moments models in terms of the soot particle number density source term. The acetylene based first-order cor-

relation of the soot nucleation rate is harmonised with a pyrene-based nucleation model [7] and experimental data from the premixed ethylene/air WSR/PFR system [9]. However, it can not *a priori* be assumed to describe soot nucleation in non-premixed systems with different fuels [62] and the sensitivity is explored below.

2.3.2 Surface Growth

Particle growth due to the adsorption of C_2H_2 on the soot surface is the dominant mechanism for increasing soot mass and is modelled via a one-step reaction [21, 22, 28].

$$C_2H_2 \longrightarrow 2\,C_{soot} + H_2 \tag{54}$$

Soot mass growth via acetylene is approximately a first order reaction [63] and a proportionality to the total external surface area of soot A_s is assumed.

$$R_G = k_G(T) A_s \left[C_2H_2\right] \tag{55}$$

The total surface is calculated under the assumption of spherical particles and, disregarding any effect of soot porosity [64, 65], from the particle number density via the surface area of an individual particle $A_p (= \pi d_p^2)$ (m^2) via Eq. (56) and Eq. (17). The approach is consistent with that used in the sectional model.

$$A_s = A_p \left[\rho N_s\right] \tag{56}$$

In the context of the method of moments, the treatment of the particle surface area is included in Eqs. (45)–(48), and the term for one-step growth given below.

$$A_G = k_G(T) \left[C_2H_2\right] \tag{57}$$

The soot mass growth step discussed above can be augmented to approximately take into account the effects of the chemical environment of the soot particle, e.g. via the ubiquitous

hydrogen-abstraction/acetylene-addition (HACA) sequence first introduced by Frenklach and Wang [66]. The current work features a closed, systematically reduced, analogy of the soot surface chemistry [28, 43] based on naphthalene, previously evaluated in the context of a plug flow reactor [67] and for the turbulent diffusion flames of Kent and Honnery [60] and Coppalle and Joyeux [61]. The expression for growth including surface chemistry effects is analogous to Eq. (55) and given by Eq. (58), where $k_X^f(T)$ is the acetylene addition rate and χ_s expresses the number of sites available for reaction on the surface of soot particles. Appendix A contains a full description of the model.

$$R_G = k_X^f(T)\chi_s A_s \left[C_2H_2\right] \tag{58}$$

For the sectional model, growth is calculated via Eq. (58) with the soot surface area defined as a function of the particle size class, rather than calculated via Eq. (56).

2.3.3 Oxidation

The oxidation of soot is assumed to take place via irreversible reactions with OH, O and O_2 as described by Eqs. (59)–(61).

$$C_{soot} + OH \longrightarrow CO + H \tag{59}$$

$$C_{soot} + O \longrightarrow CO \tag{60}$$

$$C_{soot} + O_2 \longrightarrow CO + O \tag{61}$$

Guo et al. [68] examined twelve experimental studies [69–81] reporting soot oxidation rates, temperature, OH and O_2 concentration, comprising a total of 160 measurements of soot oxidation rates in premixed flames, diffusion flames, thermogravimetric analyzers (TGAs) and flow reactors for a wide range of conditions. Optimized reaction rate expressions for oxidation of soot by OH and O_2 were developed, featuring a collision efficiency of 0.10 for soot oxidation by OH and an activation energy of 195 kJ/mol for oxidation by

O_2. The latter value is much higher than that suggested by Roth et al. [82], but comparatively close to the value of 164 kJ/mol used by Lindstedt [22]. In the current work, the reaction rate constants of Lindstedt and Louloudi [28, 43] are compared with the updated suggestion for the collision efficiency of OH from Guo et al. [68] and the rate with the higher activation barrier [22]. The combined reaction rate is given by Eqs. (62)–(63), with A_O representing the method of moments oxidation term in Eqs. (46) and (48). The form given by Eq. (63) corresponds to the source term in the two-equation and sectional models, with oxidation being considered proportional to the total soot surface area A_s, or, for the sectional model, the area associated with a particle size class.

$$A_O = \left(k_{\mathrm{OH},1}(T) \left[\mathrm{OH}\right] + k_{\mathrm{O},1}(T) \left[\mathrm{O}\right] + k_{\mathrm{O_2},1}(T) \left[\mathrm{O_2}\right] \right) \tag{62}$$

$$R_O = A_O A_s \tag{63}$$

2.4 *Dissipation Rate Closure*

The standard expression for the scalar mixing time scale τ_ϕ is related to the ratio of the turbulence kinetic energy $\widetilde{k}$ and its dissipation rate $\widetilde{\varepsilon}$,

$$\tau_\phi^{-1} = \frac{C_\phi}{2} \frac{\widetilde{\varepsilon}}{\widetilde{k}} = \frac{C_\phi}{2} \tau_T^{-1}, \tag{64}$$

assuming a uniform ratio of the local turbulence time scale τ_T and the local mixing time scale τ_ϕ in the whole domain. The parameter C_ϕ has been the subject of parametric studies and, in conjunction with Curl's mixing model, Lindstedt et al. [27, 83] proposed a value of 2.3. For the current set-up, values in the range $2.3 \leq C_\phi \leq 6.0$ were explored to facilitate sustained ignition. In the context of premixed turbulent flames, an extended closure for the scalar time scale was derived by Kuan et al. [84],

$$\tau_{\phi}^{-1} = \frac{C_{\phi}}{2}\left[1.0 + C_{\phi}^{*}\frac{\rho_u}{\bar{\rho}}\frac{u_L}{u_\eta}\right]\tau_T^{-1}, \tag{65}$$

where the ratio $\rho_u/\bar{\rho}$ expresses the ratio of the density of the unburnt reactants to the local mean density, u_L is the local laminar burning velocity, a function of the mixture fraction (or equivalence ratio), and $u_\eta = (\nu\widetilde{\varepsilon})^{1/4}$ is the local Kolmogorov velocity scale, defined by the local kinematic viscosity ν and the turbulence dissipation rate $\widetilde{\varepsilon}$. The formulation leads to a local increase of the scalar mixing frequency in regions with equivalence ratios corresponding to flammable mixtures. The closure has been validated for a range of conditions [84–87]. Lindstedt et al. [86] assessed the impact of different scalar dissipation rate closure approximations for a set of piloted partially premixed CH_4/H_2/air turbulent jet flames at Re $\approx$ 60,000 and 67,000, and the extended closure was subsequently applied to turbulent diffusion flames by Gkagkas et al. [87]. The parameter values $C_\phi = 2.3$ and $C_\phi^* = 1.2$ are retained from previous work. Laminar burning velocity data was obtained from premixed laminar flame calculations with a strain rate of $a \approx 100$ s^{-1} and is shown in Fig. 1. A sum-of-sines fit to the data in the range $0.35 \leq \Phi \leq 1.95$ was applied and implemented into the turbulent flame calculations with $u_L = 0$ elsewhere. The sensitivity of the model to the formulation of dissipation rate closure used is discussed in Section 4.

3. Case Configuration

3.1 *WSR/PFR configuration*

The WSR/PFR reactor configuration of Manzello et al. [8, 9] features a plug flow reactor connected to the outlet of a well-stirred reactor. The setup has been used to study growth of polycyclic aromatic hydrocarbons (PAHs) and soot inception by measuring soot particle size distributions (PSDs) [8, 9] under fuel-rich conditions. The resulting data is suitable for the validation of soot models aimed at reproducing PSDs under premixed conditions. Calculations are here carried out under sooting conditions for an ethylene/air mixture at

Φ = 2.0, an air flow rate of 175 SLPM, and with a temperature of 1723 K in the WSR, as reported by Lenhert et al. [9]. The temperature profile imposed in the subsequent PFR is based on the interpolation of experimental data [88].

3.2 *Delft III / Adelaide Flame*

The Delft burner is shown in Fig. 2 and features a concentric layout of a central fuel jet at Re = 9,700 with a diameter d = 6 mm at the exit plane, an annular rim of 4.5 mm width holding the pilot flame, and an annular air co-flow at Re = 8600 with inner and outer diameters of 30 and 45 mm in the fuel exit plane [31]. The burner is placed in an octagonal burner chamber in which a forced secondary air co-flow prevents recirculation. The pilot burns a mixture of acetylene, hydrogen and air, with the same elemental carbon-to-hydrogen ratio as the main fuel jet at an equivalence ratio of Φ = 1.4, and is supplied by twelve individual pilot holes of diameter 0.5 mm embedded into the rim around the fuel jet on a circle of radius 7.5 mm. It accounts for about 1 % of the total power of the flame. The mean exit velocity of the cold pilot flow is reported by de Vries [89] to be $\widetilde{U}_p$ = 12 m s^{-1}. The rim separating fuel jet and primary air co-flow, and holding the pilot flames, creates a recirculation zone near the nozzle, providing an additional flame stabilisation mechanism. The conditions lead to a flame with strong turbulence-chemistry interactions at the burner exit with some local extinction and re-ignition further downstream. The composition of the main fuel varies slightly between experiments as shown in Table 3. The RRL scalar and temperature field measurements by Nooren et al. [32, 33] were obtained using diluted Californian natural gas. As higher hydrocarbons are not included in the current chemical mechanism, their mole fractions were added to that of ethane ("Model 1") shown in Table 3. The Dutch natural gas composition used for the LDA velocity measurements by Stroomer et al. [31] is very similar. The "Model 1" composition was therefore used for all comparisons with either of these experimental datasets. The diluted

Adelaide natural gas used for the LII soot measurements by Qamar et al. [34] is modelled in the same way ("Model 2") and used in calculations for this dataset. The sensitivity of the computations to the gas composition is further discussed in Section 4.2.

Merci et al. [38] assessed the use of rigorously constructed inlet conditions in comparison to the simpler variants derived from experimental mass flow rates and LDA measurements near the inlet used by Nooren [32]. As no significant advantage was reported, the simpler conditions were used in the present case: flat profiles for velocity, turbulence kinetic energy and turbulence dissipation rate in the fuel jet ($\widetilde{U}_f = 21.9\,\mathrm{m\,s^{-1}}$, $\widetilde{k}_f = 2.2\,\mathrm{m^2\,s^{-2}}$, $\widetilde{\varepsilon}_f = 500\,\mathrm{m^2\,s^{-3}}$), and secondary air co-flow ($\widetilde{U}_{a2} = 0.4\,\mathrm{m\,s^{-1}}$, $\widetilde{k}_{a2} = 4 \times 10^{-4}\,\mathrm{m^2\,s^{-2}}$, $\widetilde{\varepsilon}_{a2} = 2 \times 10^{-4}\,\mathrm{m^2\,s^{-3}}$), and the profiles in the primary air co-flow were based on a fully developed annulus flow calculation with bulk velocity $\widetilde{U}_{a1} = 4.3\,\mathrm{m\,s^{-1}}$. Across the pilot rim, the axial velocity profile in the inlet plane drops linearly from $21.9\,\mathrm{m\,s^{-1}}$ at the edge of the fuel jet to $1\,\mathrm{m\,s^{-1}}$ at a radial position $y = 3.7\,\mathrm{mm}$ and remains at this value for $y \leq 7.5\,\mathrm{mm}$. The inlet axial velocity profile in the primary air co-flow is flattened by a factor of 0.96 to account for the additional momentum introduced in the computation. The turbulence kinetic energy k across the rim is taken to vary linearly from the value in the fuel jet to zero at the outer edge of the rim. The turbulence dissipation rate is approximated from a dimensional argument as $\varepsilon_{max} = \sqrt{2/3}k^{3/2}l_t^{-1}$, with the turbulence length scale l_t set to the rim width (9 mm).

The pilot of the Delft flame is modelled by introducing a volumetric enthalpy source in a region close to the burner exit, while omitting the pilot flow, as chosen by Merci et al. [38] for the same flame. The pilot flame being responsible for only about 1 % of the burner's total power output, omitting its mass flow is not expected to alter downstream results considerably. The volume occupied by the heat source is defined by an annulus located at the inner boundary of the pilot rim in the exit plane of the burner and with an axial extension x as $3.0 \leq y \leq 4.5\,\mathrm{mm}$, $0 \leq x \leq 7.5\,\mathrm{mm}$.

The computations featured 465 distributed radial control volumes with 275 in the core jet, 70 in the pilot and 120 in the coflow. The cells were dynamically redistributed during computation based on the evolution of the stream function in physical space, ensuring sufficient resolution in the main reaction zone as the jet expands. The computations featured a minimum of 200 stochastic particles per cell and were performed using 20 cores.

4. Results and Discussion

4.1 *WSR/PFR configuration*

Measured [9] and predicted soot particle size distributions (PSDs) obtained with the sectional model in the well-stirred reactor and at ports 1 and 3 of the plug flow reactor are presented in Fig. 3, with the rate parameters for the nucleation steps shown in Table 4, and for other reaction steps, including soot oxidation, in Table 5. Soot oxidation was modelled via the updated rates (k_O, $k_{OH,2}$, $k_{O_2,2}$). The modes of the measured and calculated PSDs in the WSR and at Ports 1 and 3 of the PFR are shown in Table 6. The measured modes in the PFR are almost identical, while the computations show an evolution towards larger particles. For a surface reactivity parameter $\alpha_s = 0.85$, the pyrene based nucleation model by Lindstedt and Waldheim [7] agrees well with measurements. Nucleation rate $k_{N,1}$ results in calculated modes that are more than double the experimental data. This is consistent with the observations of Sunderland et al. [57, 59] and Lin et al. [58] who report the rate used by Leung et al. [21] ($\approx 1.6 \times k_{N,1}$) to be excessively high. The discrepancy is related to scarcity of experimental data and uncertainties in the interpretation of optical measurements used to evaluate primary particle sizes at the time [57]. Results from calculations using $k_{N,2}$ [59] show better agreement. The modes in the WSR and at PFR Port 3 are overpredicted by around 30% and 40%, respectively. Acceptable agreement with the acetylene based nucleation model is obtained using $k_{N,3}$ and $k_{N,4}$, with the for-

mer matching the predictions from the pyrene based model closely. The pre-exponential factors for $k_{N,5}$ and $k_{N,6}$ were further reduced by factors of 2 and 4, compared to $k_{N,4}$, to explore the sensitivity. The modes in the WSR are similar for $k_{N,3}$ to $k_{N,6}$ and overpredict the measured value by 14%. At PFR Port 3, the measured value is overpredicted by 6% for pyrene-based nucleation. For the acetylene-based model, $k_{N,3}$ and $k_{N,4}$ underpredict the experiment by 8%. A further reduction in the nucleation rate leads to deteriorating agreement with the predicted modes being 19% ($k_{N,5}$) and 29% ($k_{N,6}$) lower than the experiment. Figure 4 shows PSDs obtained using the rates $k_{N,3}$ and $k_{N,4}$ and the alternative oxidation rates ($k_{OH,1}$, $k_{O_2,1}$). The results are virtually identical to those of Fig. 3.

4.2 *Delft III / Adelaide Flame*

The sensitivity of computed results for the Delft III / Adelaide flame due to the pilot power and the dissipation rate closure was explored. For the latter, calculations using the standard scalar dissipation rate closure (Eq. (64)) were performed with $2.3 \leq C_\phi \leq 6.0$ and the unchanged extended closure (Eq. (65)). Each case was calculated with a pilot power corresponding to the experimental value of 196 W and increased by factors of 1.25 (245 W) and 1.50 (294 W). For the standard closure, global flame extinction was observed at $x/d \leq 17$ for $C_\phi = 2.3$ for the above pilot powers. For $C_\phi = 4.0$, flame extinction was observed for 196 W and 245 W with the point of extinction shifting downstream to $17 \leq x/d \leq 25$. Global extinction was not observed for $C_\phi = 6.0$. The behaviour is consistent with the excessive flame extinction found by Lindstedt et al. [86] for partially premixed flames. By contrast, the extended closure was found to generally avoid global extinction. Merci et al. [38, 39] and Roekaerts et al. [40] also observed excessive local extinction with the Curl's model and the standard dissipation rate model ($C_\phi = 2.0$) and increased the pilot power by 50%. Given the small contribution (≈ 1 %) of the pilot to the total thermal power of the flame, an increase in pilot power to 245 W is considered

reasonable to aid flame stability in the stochastic calculations. However, results obtained with the experimental value of 196 W are also presented. Unless otherwise stated, all results presented were obtained using the extended closure for the scalar dissipation rate and a pilot power of 245 W. To match the experimental conditions, the diluted Californian natural gas defined in Table 3 ("Model 1") was used for calculations of velocity and scalar fields shown in Fig. 5–7 and 18 and the Adelaide gas composition ("Model 2") is used for comparisons with measured soot data in Fig. 13–17 and 19–20. The impact of the gas composition on soot predictions is further discussed in the context of Fig. 13–14.

Figures 5–7 show radial profiles of Favre mean axial velocity ($\widetilde{U}$), RMS of axial (u'') and radial (v'') velocities, mixture fraction (f) and temperature (T) in the Delft flame. The agreement between computations and experiments is overall arguably fair, although there is a tendency to over-predict v'' throughout and u'' far downstream from the burner exit. The correspondence between the computed and measured mixture fraction statistics is generally good, although f'' is over-predicted in the jet centre near the nozzle and the variance peaks in the jet flanks at $x/d = 41\frac{2}{3}$ are somewhat too low. Further, the temperatures at the outer edges of the core jet are predicted to be higher as shown, for example, at $x/d \leq 8\frac{1}{3}$ and $x/d = 41\frac{2}{3}$. The peak temperature is also overpredicted, while the location is in reasonable agreement. The discrepancies can in part be attributed to the boundary conditions across the pilot rim, in conjunction with the parabolic CFD solver, not correctly reflecting the downstream effect of the small recirculation zone. By comparison, the velocity and scalar fields reported by LES simulations [35, 36] show improved agreement for velocity and temperature statistics.

The prediction of the H_2O mass fractions mirrors the temperature data to some extent as shown in Fig. 8 with reduced accuracy in the jet flanks at $x/d = 33\frac{1}{3}$ and $x/d = 41\frac{2}{3}$. Computed mass fractions of H_2 suggest too high peak values close to the burner exit with improved agreement further downstream (Fig. 9). The inaccuracies in the jet flanks,

noted for temperature and water, are not present for hydrogen. This suggests that the reaction zone structure is comparatively well reproduced. The computed CH_4 mass fractions shown in Fig. 10 appear to support this suggestion. The observation is important as soot formation is expected to occur in fuel rich mixtures towards the fuel jet and not in the leaner mixtures in the jet flanks. Computed CO mass fractions show a tendency to over-predict the mean at the peaks for $x/d \leq 16\frac{2}{3}$ and also in the centre of the jet further downstream as shown in Fig. 11. The computed mass fraction statistics for OH are presented in Fig. 12. The RMS fluctuations are of the same order as the mean and the data is hence presented separately for clarity. The peak location is well reproduced along with the extent of the reaction zone with peak values showing a tendency to being over predicted as expected from the computed temperatures.

From a soot nucleation chemistry point of view, the change of fuel from C_2H_4 to (effectively) CH_4 presents a significant step. Calculations of the Delft flame were accordingly obtained for nucleation rates $k_{N,3}$, $k_{N,4}$ and $k_{N,6}$, based on (i) matching of the PSD data for ethylene in the WSR/PFR geometry and (ii) a potentially reduced rate for methane. The influence of the fuel composition, the pilot power and the dissipation rate closure on the calculated mean soot volume fraction at the centreline is shown in Fig. 13–14. The two-equation model with the additional PAH analogy for surface growth (Eq. (58)), combined with oxidation rates k_O, $k_{OH,2}$, $k_{O_2,2}$, is used as the base case for comparisons with the experimental data from Qamar et al. [34]. In Fig. 13, the predicted Favre mean soot volume fraction ($\widetilde{f_v}$) at the centreline using the "Model 2" gas composition in the fuel jet, the experimental pilot power (196 W) and the extended scalar dissipation rate closure provides a reference (green lines). The value of the surface reactivity parameter $\alpha_s = 0.85$ is kept consistent with the WSR/PFR calculations, and the nucleation rate $k_{N,6}$ is used. The peak value of the soot volume fraction at the centreline is approximately in agreement with the experimental data, while its locations is predicted approximately

40 nozzle diameters upstream. The location is consistent with the LES (combined with a flamelet / progress variable approach and a hybrid method of moments model) calculations by Mueller and Pitsch [35] and Donde et al. [36]. The soot volume fraction displays little sensitivity to the gas composition (left panel), confirming that the minor variations in the fuel compositions are not important. The influence of the pilot model is shown in the centre panel. An increase in the peak soot value is observed if the pilot power is increased from the experimental value, along with a marked overprediction of soot far upstream at $x/d \leq 50$. Lindstedt and Louloudi [28, 43] obtained ignition for the turbulent diffusion flames of Kent and Honnery [60] and Coppalle and Joyeux [61] using a presumed PDF / flamelet approach in the region close to the nozzle and increased soot levels far upstream were not observed. This points to a high sensitivity of the surface growth model to the locally elevated temperature and radical concentrations caused by the pilot. The standard scalar dissipation rate closure with $C_\phi = 6.0$ (right panel) increases mixing in the whole flow domain, resulting in a slightly increased peak values of soot.

As discussed above, calculations of PSDs in the WSR/PFR system using $k_{N,6}$ underestimate the soot formation, while $k_{N,3}$ and $k_{N,4}$ yield similar agreement as the detailed chemistry calculation with pyrene nucleation. In Fig. 14, the sensitivity of soot predictions to different model parameters is shown for the higher nucleation rate $k_{N,4}$ and the surface reactivity parameter reduced to $\alpha_s = 0.50$. The calculated peak soot value with a pilot power of 245 W is similar to that discussed above. However, the use of $\alpha_s = 0.85$ with the higher nucleation rate ($k_{N,4}$) results in an overprediction of the peak soot by a factor of 3. The sensitivity discussed in the context of Fig. 13 is approximately reproduced with peak soot values only moderately increased with pilot power. The corresponding sensitivity to the particle dynamics, growth models, oxidation and nucleation rates is shown in Fig. 15–17. Predictions obtained with the two-equation model and one-step growth are shown in Fig. 15. The upstream shift in peak soot location discussed above is reproduced. The same

phenomenon was observed in the LES calculations by Mueller and Pitsch [35] and Donde et al. [36] was attributed the cause to uncertainties in the PAH chemistry. However, the nucleation rate in the current model was chosen to be consistent with that of pyrene in the WSR/PFR geometry, as discussed above, and found to reasonably predict the soot PSD. Furthermore, while the peak soot volume fraction increased by a factor of approximately 30 with the use of $k_{N,1} = 167 \cdot k_{N,4}$, the axial location of the soot peak only moves in the range $x/d \approx 77.2$ to $x/d \approx 80.1$ (for the two-equation model and $k_{OH,2}$, $k_{O_2,2}$) and is hence broadly independent of the nucleation rate. The calculated soot volume fraction is virtually identical for either set of soot oxidation rates ($k_{OH,1}$, $k_{O_2,1}$ or $k_{OH,2}$, $k_{O_2,2}$) and $k_{N,3}$, while peak soot is moderately reduced for $k_{OH,2}$, $k_{O_2,2}$ and $k_{N,4}$. A corresponding data set for the soot volume fraction obtained with the method of moments by solving for the first four moments ($M_0 - M_3$) of the soot PSDF is presented in Fig. 16. The agreement with experimental data is similar to that obtained with the two-equation model, albeit with a tendency to lower peak values.

Figure 17 shows computations using the two-equation model with the additional PAH analogy model for soot surface growth (Eq. (58)). As for the calculations presented in Fig. 13–14, soot levels are increased for $x/d \leq 50$ due to the sensitivity of the extended growth model to the pilot treatment. Again, no strong sensitivity to the oxidation rates is observed, with moderately reduced soot levels obtained for $k_{OH,2}$ and $k_{O_2,2}$. As for the method of moments calculations, the sensitivity to the nucleation rate appears reduced in comparison to the two-equation model calculations without the PAH analogy model for soot growth, and the measured peak soot volume fraction at the centreline is approximately matched for $k_{N,4}$. The LES simulations by Mueller and Pitsch [35] and Donde et al. [36] provide overall superior flow field predictions. However, the peak soot levels were found to be (strongly) influenced by the subfilter dissipation rate model with over-predictions by factors of 3–5.5 [35] and 6.5 [36] reported. It can also be noted that despite

the very different computational methods applied, the centreline peak soot location varies approximately in the range $72 \leq x/d \leq 80$, compared to the experimental location of ≈ 116. In this context, the current results are encouraging and the compatibility of the simplified nucleation rate across different fuels and devices perhaps surprising with the optimal nucleation rate for each case differing by around a factor of 4.

Figure 18 shows the downstream evolution of the computed and measured Favre mean mixture fraction at the centreline. The black line corresponds to the case shown in the bottom right panel of Fig. 17. No effect of the fuel stream composition on the mixture fraction profile was observed and the results are omitted here. The influence of the pilot source term and the dissipation rate closure is shown in Figs. 18(a) and 18(b), respectively. The experimental data is reasonably well reproduced. A change in the pilot power from 196 W to 294 W or the use of the standard dissipation rate closure ($C_\phi = 6.0$) result in minor variations in the calculated mean mixture fraction. The locations of the computed and measured soot peaks are also indicated.

Figure 19 shows the measured and calculated values of the mean soot volume fraction against the calculated mixture fraction on the centreline. The computations shown were obtained with the two-equation model with the growth step given by Eq. (54) and with the PAH analogy for the soot surface chemistry with $\alpha_s = 0.50$ via Eq. (58). The data is compared to the lean (f_{LFL}) and rich (f_{RFL}) flammability limits of methane, and the stoichiometric mixture fraction f_{st} of the Adelaide natural gas, calculated as $f_{st} \approx 0.073$ via the formula of Bilger et al. [90]. The peak mean soot is predicted on the rich side of stoichiometry at $f \approx 0.11$, with no soot present below f_{LFL} and some transported soot at $f > f_{RFL}$. On the other hand, the peak of the measured mean soot is located at $f \approx 0.05$, below the stoichiometric mixture fraction, with some soot present below the lean flammability limit. The absence of experimental mixture fraction data for this part of the flame introduces uncertainties in the mapping of the measurements to the computed mixture

fraction space. Predictions of the mean mixture fraction at the centreline for $x/d \leq 41\frac{2}{3}$ agree reasonably well with the experimental data though a slightly lower value is noted at the final measurement point. It may be speculated that the decay of the calculated profile is exaggerated further downstream and this would result in a shift towards leaner compositions. However, it appears unlikely that the apparent discrepancy of the soot location in mixture fraction space can be attributed to such an effect as this would require an essentially constant value of the mean mixture fraction in the range $82 \leq x/d \leq 116$. Furthermore, the LES of Mueller et al. [35] and Donde et al. [36] report a slight overprediction at the final position while the axial peak soot locations remain broadly consistent with the current work. Caution therefore appears to be required when attributing the misaligned peak soot locations to specific model aspects.

Radial profiles of the Favre mean soot volume fraction are presented in Figure 20. In order to be able to compare the calculated radial distribution of soot to the measurements, given the different peak soot location, the experimental data is compared to predicted profiles at locations further upstream by using a normalisation of the radial coordinate accounting for the rate of spread of the jet. Hence, the radial positions (y) are normalised by the half-width of the jet (δ). The latter value is calculated from the profile of the predicted mean mixture fraction $\widetilde{f}$ at any given axial position (x) as $\delta = 2 \cdot y_{half}$, where $\widetilde{f}(y_{half})\big|_x = 0.5 \cdot \widetilde{f}_{max}\big|_x$. It therefore corresponds to the radial location where the mixture fraction takes a value of half the maximum $\widetilde{f}_{max}\big|_x$. The normalisation of the measured profiles of soot volume fraction is effected via the calculated mixture fraction. The calculations were obtained via the two-equation model with oxidation rates $k_{OH,2}$ and $k_{O_2,2}$, and correspond to the cases shown in the bottom right panels of Fig. 15 (using $k_{N,4}$ with one-step soot growth, red lines) and Fig. 16 ($k_{N,4}$ with PAH analogy surface growth and $\alpha_s = 0.50$, blue lines), and the reference case presented in Fig. 13 ($k_{N,6}$, $\alpha_s = 0.85$, orange lines). While the comparison is clearly approximate, it illustrates that the radial distribu-

tion of soot generally agrees with experimental data with a tendency to lower values of $\widetilde{f_v}$ in the jet flanks. In addition, the calculated oxidation of soot appears to be somewhat over-predicted.

5. Conclusions

A sectional approach [6, 7] was used to determine an approximate acetylene based soot nucleation rate that is broadly consistent with experimental data for the evolution of the soot PSD in the WSR/PFR configuration of Manzello et al. [8, 9] and that computed using pyrene as the nucleating species [7]. The rate was then applied directly to the modelling of the Delft III / Adelaide turbulent natural gas flame using a transported PDF based approach combined with two-equation and method moment based methods [15] for the soot particle dynamics. The sensitivity of computed soot levels was assessed for both geometries. Results show that the derived nucleation rate provides broadly consistent results for both cases despite parent fuels (CH_4 and C_2H_4) with very different sooting characteristics in very different experimental geometries. While the generality of such simplified descriptions remains conjectural, the current results suggests that it may be possible to derive simplified descriptions of greater applicability than expected. It is further shown that while the magnitude of the soot concentration in the flame is dependent on the nucleation rate, the physical downstream location where soot appears is broadly unaffected. It was also confirmed that previous rates for the acetylene based nucleation model [21, 22] are too high as suggested by Sunderland et al. [57, 59] and Lin et al. [58]. An update of the soot oxidation model used in previous work [6, 28], to reflect the recent evaluation by Guo et al. [68], was found to have only a minor impact on the predicted soot PSDs in the WSR/PFR configuration and a moderate influence in the Delft flame. The agreement obtained for the latter for velocity, temperature and the mass fractions of major species with measurements by Stroomer et al. [31] and Nooren et al. [32, 33] was found to be

fair with some discrepancies close to the nozzle attributed to the pilot model. Acceptable quantitative agreement with experimental soot measurements by Qamar et al. [34] was found, with the maximum soot volume fraction at the centreline approximately matched for the two-equation and the method of moments based approaches. The computed radial profiles of soot were compared with experimental data by accounting for the rate of spread of the jet by tracking the location where the mixture fraction reaches 50% of its maximum value at a each radial location. The resulting comparisons are tentative, but show arguably good agreement between computations and measurements. The impact of the inclusion of the PAH based analogy for soot surface reactions by Lindstedt and Louloudi [28] was also evaluated. For a value of the surface reactivity parameter α_s = 0.85, consistent with the WSR/PFR calculations, a further reduction of the nucleation rate by approximately a factor of 4 is required to match soot levels in the Delft (methane) flame. The application of the unadjusted rate results in an overprediction of the peak soot level by around a factor of 3. The values $0.50 \leq \alpha_s \leq 0.85$ compare to 0.75–1.0 used by Lindstedt and Louloudi [28] for turbulent non-premixed ethylene flames and 0.2–0.6 reported by Kazakov et al. [91] for laminar premixed ethylene flames.

Acknowledgments

The authors wish to gratefully acknowledge the support of the European Commission under Grant JTI-CS-2013-01-SAGE-06-004 (project number 620143). The authors wish to thank Prof. Dirk Roekaerts at TU Delft and Dr. Shaun Chan at the University of New South Wales for providing the experimental data.

References

[1] M. von Smoluchowski, *Three lectures on diffusion, Brownian movement and coagulation of colloidal particles*, Phys. Zeitschrift 17 (1916), pp. 557–571, 585–599.

[2] F. Gelbard, Y. Tambour, and J.H. Seinfeld, *Sectional representations for simulating aerosol dynamics*, J. Colloid Interface Sci. 76 (1980), pp. 541–556.

[3] T.T. Nguyen, F. Laurent, R.O. Fox, and M. Massot, *Solution of population balance equations in applications with fine particles: Mathematical modeling and numerical schemes*, J. Comput. Phys. 325 (2016), pp. 129–156.

[4] M.D. Smooke, M.B. Long, B.C. Connelly, M.B. Colket, and R.J. Hall, *Soot formation in laminar diffusion flames*, Combust. Flame 143 (2005), pp. 613–628.

[5] S. Kumar and D. Ramkrishna, *On the solution of population balance equations by discretization–I. A fixed pivot technique*, Chem. Eng. Sci. 51 (1996), pp. 1311–1332.

[6] J.S. Bhatt and R.P. Lindstedt, *Analysis of the impact of agglomeration and surface chemistry models on soot formation and oxidation*, Proc. Combust. Inst. 32 (2009), pp. 713–720.

[7] R.P. Lindstedt and B.B.O. Waldheim, *Modeling of soot particle size distributions in premixed stagnation flow flames*, Proc. Combust. Inst. 34 (2013), pp. 1861–1868.

[8] S.L. Manzello, D.B. Lenhert, A. Yozgatligil, M.T. Donovan, G.W. Mulholland, M.R. Zachariah, and W. Tsang, *Soot particle size distributions in a well-stirred reactor/plug flow reactor*, Proc. Combust. Inst. 31 (2007), pp. 675–683.

[9] D.B. Lenhert and S.L. Manzello, *Effects of benzene and naphthalene addition on soot inception in a well-stirred reactor/plug flow reactor*, Proc. Combust. Inst. 32 (2009), pp. 657–664.

[10] A.D. Abid, N. Heinz, E.D. Tolmachoff, D.J. Phares, C.S. Campbell, and H. Wang, *On evolution of particle size distribution functions of incipient soot in premixed ethylene–oxygen–argon flames* Combust. Flame 154 (2008), pp. 775–788.

[11] A.D. Abid, E.D. Tolmachoff, D.J. Phares, H. Wang, Y. Liu, and A. Laskin, *Size distribution and morphology of nascent soot in premixed ethylene flames with and without benzene doping*, Proc. Combust. Inst. 32 (2009), pp. 681–688.

[12] A.D. Abid, J. Camacho, D.A. Sheen, and H. Wang, *Quantitative measurement of soot particle size distribution in premixed flames – The burner-stabilized stagnation flame approach*, Combust. Flame 156 (2009), pp. 1862–1870.

[13] S.H. Park and S.N. Rogak, *A novel fixed-sectional model for the formation and growth of aerosol agglomerates*, J. Aerosol Sci. 35 (2004), pp. 1385–1404.

[14] M. Frenklach and S.J. Harris, *Aerosol dynamics modeling using the method of moments*, J. Colloid Interface Sci. 118 (1987), pp. 252–261.

[15] M. Frenklach, *Method of moments with interpolative closure*, Chem. Eng. Sci. 57 (2002), pp. 2229–2239.

[16] R. McGraw, *Description of aerosol dynamics by the quadrature method of moments*, Aerosol Sci. Technol. 27 (1997), pp. 255–265.

[17] D.L. Marchisio and R.O. Fox, *Solution of population balance equations using the direct quadrature method of moments*, J. Aerosol Sci. 36 (2005), pp. 43–73.

[18] M.E. Mueller, G. Blanquart, and H. Pitsch, *Hybrid Method of Moments for modeling soot formation and growth*, Combust. Flame 156 (2009), pp. 1143–1155.

[19] C. Yuan and R.O. Fox, *Conditional quadrature method of moments for kinetic equations*, J. Comput. Phys. 230 (2011), pp. 8216–8246.

[20] S. Salenbauch, A. Cuoci, A. Frassoldati, C. Saggese, T. Faravelli, and C. Hasse, *Modeling soot formation in premixed flames using an Extended Conditional Quadrature Method of Moments*, Combust. Flame 162 (2015), pp. 2529–2543.

[21] K.M. Leung, R.P. Lindstedt, and W.P. Jones, *A simplified reaction mechanism for soot formation in nonpremixed flames*, Combust. Flame 87 (1991), pp. 289–305.

[22] R.P. Lindstedt, *Simplified soot nucleation and surface growth steps for non-premixed flames*, in *Soot Formation in Combustion: Mechanisms and Models*, H. Bockhorn, ed., Springer-Verlag, 1994, pp. 417–441.

[23] M. Fairweather, W.P. Jones, H.S. Ledin, and R.P. Lindstedt, *Predictions of soot formation in turbulent, non-premixed propane flames*, Proc. Combust. Inst. 24 (1992), pp. 1067–1074.

[24] M. Fairweather, W.P. Jones, and R.P. Lindstedt, *Predictions of radiative transfer from a turbulent reacting jet in a cross-wind*, Combust. Flame 89 (1992), pp. 45–63.

[25] S.B. Pope, *PDF methods for turbulent reactive flows*, Prog. Energy Combust. Sci. 11 (1985), pp. 119–192.

[26] P.P. Popov and S.B. Pope, *Large eddy simulation/probability density function simulations of bluff body stabilized flames*, Combust. Flame 161 (2014), pp. 3100–3133.

[27] R.P. Lindstedt and S.A. Louloudi, *Joint scalar transported probability density function modeling of turbulent methanol jet diffusion flames*, Proc. Combust. Inst. 29 (2002), pp. 2147–2154.

[28] R.P. Lindstedt and S.A. Louloudi, *Joint-scalar transported PDF modeling of soot formation and oxidation*, Proc. Combust. Inst. 30 (2005), pp. 775–782.

[29] T.W.J. Peeters, P.P.J. Stroomer, J.E. de Vries, D.J.E.M. Roekaerts, and C.J. Hoogendoorn, *Comparative experimental and numerical investigation of a piloted turbulent natural-gas diffusion flame*, Proc.

Combust. Inst. 25 (1994), pp. 1241–1248.

[30] The University of Adelaide, *International Sooting Flame (ISF) Workshop*, http://www.adelaide.edu.au/cet/isfworkshop/.

[31] P.P.J. Stroomer, J.E. de Vries, and T.H. van der Meer, *Effects of small- and large-scale structures in a piloted jet diffusion flame*, Flow, Turbul. Combust. 62 (1999), pp. 53–68.

[32] P.A. Nooren, *Stochastic modeling of turbulent natural-gas flames*, Ph.D. thesis, Delft University of Technology, 1998.

[33] P.A. Nooren, M. Versluis, T.H. van der Meer, R.S. Barlow, and J.H. Frank, *Raman-Rayleigh-LIF measurements of temperature and species concentrations in the Delft piloted turbulent jet diffusion flame*, Appl. Phys. B Lasers Opt. 71 (2000), pp. 95–111.

[34] N.H. Qamar, Z.T. Alwahabi, Q.N. Chan, G.J. Nathan, D. Roekaerts, and K.D. King, *Soot volume fraction in a piloted turbulent jet non-premixed flame of natural gas*, Combust. Flame 156 (2009), pp. 1339–1347.

[35] M.E. Mueller and H. Pitsch, *LES model for sooting turbulent nonpremixed flames*, Combust. Flame 159 (2012), pp. 2166–2180.

[36] P. Donde, V. Raman, M.E. Mueller, and H. Pitsch, *LES/PDF based modeling of soot-turbulence interactions in turbulent flames*, Proc. Combust. Inst. 34 (2013), pp. 1183–1192.

[37] P.A. Nooren, H.A. Wouters, T.W.J. Peeters, D. Roekaerts, U. Maas, and D. Schmidt, *Monte Carlo PDF modelling of a turbulent natural-gas diffusion flame*, Combust. Theory Model. 1 (1997), pp. 79–96.

[38] B. Merci, B. Naud, and D. Roekaerts, *Flow and mixing fields for transported scalar PDF Simulations of a piloted jet diffusion flame ('Delft Flame III')*, Flow, Turbul. Combust. 74 (2005), pp. 239–272.

[39] B. Merci, D. Roekaerts, and B. Naud, *Study of the performance of three micromixing models in transported scalar PDF simulations of a piloted jet diffusion flame ("Delft Flame III")*, Combust. Flame 144 (2006), pp. 476–493.

[40] D. Roekaerts, B. Merci, and B. Naud, *Comparison of transported scalar PDF and velocity-scalar PDF approaches to 'Delft flame III'*, Comptes Rendus Mécanique 334 (2006), pp. 507–516.

[41] A. Habibi, B. Merci, and D. Roekaerts, *Turbulence radiation interaction in Reynolds-averaged Navier-Stokes simulations of nonpremixed piloted turbulent laboratory-scale flames*, Combust. Flame 151 (2007), pp. 303–320.

[42] S. Ayache and E. Mastorakos, *Conditional Moment Closure/Large Eddy Simulation of the Delft-III natural gas non-premixed jet flame*, Flow, Turbul. Combust. 88 (2012), pp. 207–231.

[43] S.A. Louloudi, *Transported probability density function modeling of turbulent jet flames*, Ph.D. thesis, Imperial College London, 2003.

[44] D.B. Spalding, *GENMIX – A General Computer Program for Two-Dimensional Parabolic Phenomena*, Pergamon Press, Oxford, 1977.

[45] C.G. Speziale, S. Sarkar, and T.B. Gatski, *Modelling the pressure-strain correlation of turbulence: An invariant dynamical systems approach*, J. Fluid Mech. 227 (1991), pp. 245–272.

[46] B.J. Daly and F.H. Harlow, *Transport equations in turbulence*, Phys. Fluids 13 (1970), pp. 2634–2649.

[47] J. Janicka, W. Kolbe, and W. Kollmann, *Closure of the transport equation for the probability density function of turbulent scalar fields*, J. Non-Equilibrium Thermodyn. 4 (1979), pp. 47–66.

[48] W.L. Grosshandler, *RADCAL: A Narrow-Band Model for Radiation Calculations in a Combustion Environment.*, Tech. Rep., NIST Technical Note 1402, 1993.

[49] R.J. Hall, *Computation of the radiative power loss in a sooting diffusion flame*, Appl. Opt. 27 (1988), pp. 809–811.

[50] M. Frenklach and H. Wang, *Detailed mechanism and modeling of soot particle formation*, in *Soot Formation in Combustion: Mechanisms and Models*, H. Bockhorn, ed., Springer-Verlag, 1994, pp. 165–192.

[51] A. Kazakov and M. Frenklach, *Dynamic modeling of soot particle coagulation and aggregation: Implementation with the method of moments and application to high-pressure laminar premixed flames*, Combust. Flame 114 (1998), pp. 484–501.

[52] S.E. Pratsinis, *Simultaneous nucleation, condensation, and coagulation in aerosol reactors*, J. Colloid Interface Sci. 124 (1988), pp. 416–427.

[53] Ü.Ö. Köylü, G.M. Faeth, T.L. Farias, and M.G. Carvalho, *Fractal and projected structure properties of soot aggregates*, Combust. Flame 100 (1995), pp. 621–633.

[54] S. Vemury and S.E. Pratsinis, *Self-preserving size distributions of agglomerates*, J. Aerosol Sci. 26 (1995), p. 1995.

[55] S.K. Friedlander, *Smoke, Dust, and Haze*, 2nd ed., Oxford University Press, New York, 2000.

[56] W.P. Jones and R.P. Lindstedt, *Global reaction schemes for hydrocarbon combustion*, Combust. Flame 73 (1988), pp. 233–249.

[57] P.B. Sunderland, Ü.Ö. Köylü, and G.M. Faeth, *Soot formation in weakly buoyant acetylene-fueled laminar jet diffusion flames burning in air*, Combust. Flame 100 (1995), pp. 310–322.

[58] K. Lin, P.B. Sunderland, and G.M. Faeth, *Soot nucleation and growth in acetylene air laminar coflowing*

jet diffusion flames Combust. Flame 104 (1996), pp. 369–375.

[59] P.B. Sunderland and G.M. Faeth, *Soot formation in hydrocarbon air laminar jet diffusion flames*, Combust. Flame 105 (1996), pp. 132–146.

[60] J.H. Kent and D. Honnery, *Soot and mixture fraction in turbulent diffusion flames*, Combust. Sci. Technol. 54 (1987), pp. 383–398.

[61] A. Coppalle and D. Joyeux, *Temperature and soot volume fraction in turbulent diffusion flames: Measurements of mean and fluctuating values*, Combust. Flame 96 (1994), pp. 275–285.

[62] F. Xu, K.C. Lin, and G.M. Faeth, *Soot formation in laminar premixed methane/oxygen flames at atmospheric pressure*, Combust. Flame 115 (1998), pp. 195–209.

[63] S.J. Harris and A.M. Weiner, *Determination of the rate constant for soot surface*, Combust. Sci. Technol. 32 (1983), pp. 267–275.

[64] O.B. Popovitcheva, N.M. Persiantseva, M.E. Trukhin, G.B. Rulev, N.K. Shonija, Y. Ya. Buriko, A.M. Starik, B. Demirdjian, D. Ferry, and J. Suzanne, *Experimental characterization of aircraft combustor soot: Microstructure, surface area, porosity and water adsorption*, Phys. Chem. Chem. Phys. 2 (2000), pp. 4421–4426.

[65] K.J. Rockne, G.L. Taghon, and D.S. Kosson, *Pore structure of soot deposits from several combustion sources*, Chemosphere 41 (2000), pp. 1125–1135.

[66] M. Frenklach and H. Wang, *Detailed modelling of soot particle nucleation and growth*, Proc. Combust. Inst. 23 (1990), pp. 1559–1566.

[67] M.L. Potter, *Detailed chemical kinetic modelling of propulsion fuels*, Ph.D. thesis, Imperial College London, 2003.

[68] H. Guo, P.M. Anderson, and P.B. Sunderland, *Optimized rate expressions for soot oxidation by OH and O_2*, Fuel 172 (2016), pp. 248–252.

[69] K.B. Lee, M.W. Thring, and J.M. Beér, *On the rate of combustion of soot in a laminar soot flame*, Combust. Flame 6 (1962), pp. 137–145.

[70] C.P. Fenimore and G.W. Jones, *Oxidation of soot by hydroxyl radicals*, J. Phys. Chem. 71 (1967), pp. 593–597.

[71] K.G. Neoh, *Soot burnout in flames*, Ph.D. thesis, Massachusetts Institute of Technology, 1980.

[72] M.L. Chan, K.N. Moody, J.R. Mullin, and A. Williams, *Low-temperature oxidation of soot*, Fuel 66 (1987), pp. 1694–1698.

[73] A. Garo, G. Prado, and J. Lahaye, *Chemical aspects of soot particles oxidation in a laminar methane-air diffusion flame*, Combust. Flame 79 (1990), pp. 226–233.

[74] R. Puri, R.J. Santoro, and K.C. Smyth, *The oxidation of soot and carbon monoxide in hydrocarbon diffusion flames*, Combust. Flame 97 (1994), pp. 125–144.

[75] R. Puri, R.J. Santoro, and K.C. Smyth, *Erratum*, Combust. Flame 102 (1995), pp. 226–228.

[76] K.J. Higgins, H. Jung, D.B. Kittelson, J.T. Roberts, and M.R. Zachariah, *Size-selected nanoparticle chemistry: Kinetics of soot oxidation*, J. Phys. Chem. A 106 (2002), pp. 96–103.

[77] F. Xu, A.M. El-Leathy, C.H. Kim, and G.M. Faeth, *Soot surface oxidation in hydrocarbon/air diffusion flames at atmospheric pressure*, Combust. Flame 132 (2003), pp. 43–57.

[78] C.H. Kim, A.M. El-Leathy, F. Xu, and G.M. Faeth, *Soot surface growth and oxidation in laminar diffusion flames at pressures of 0.1–1.0 atm*, Combust. Flame 136 (2004), pp. 191–207.

[79] C.H. Kim, F. Xu, and G.M. Faeth, *Soot surface growth and oxidation at pressures up to 8.0 atm in laminar nonpremixed and partially premixed flames*, Combust. Flame 152 (2008), pp. 301–316.

[80] M. Kalogirou and Z. Samaras, *Soot oxidation kinetics from TG experiments*, J. Therm. Anal. Calorim. 99 (2010), pp. 1005–1010.

[81] H.N. Sharma, L. Pahalagedara, A. Joshi, S.L. Suib, and A.B. Mhadeshwar, *Experimental study of Carbon black and diesel engine soot oxidation kinetics using thermogravimetric analysis*, Energy and Fuels 26 (2012), pp. 5613–5625.

[82] P. Roth, O. Brandt, and S. von Gersum, *High temperature oxidation of suspended soot particles verified by CO and CO_2 measurements*, Proc. Combust. Inst. 23 (1990), pp. 1485–1491.

[83] R.P. Lindstedt, S.A. Louloudi, and E.M. Váos, *Joint scalar probability density function modeling of pollutant formation in piloted turbulent jet diffusion flames with comprehensive chemistry*, Proc. Combust. Inst. 28 (2000), pp. 149–156.

[84] T.S. Kuan, R.P. Lindstedt, and E.M. Váos, *Higher moment based modeling of turbulence enhanced explosion kernels in confined fuel-air mixtures*, in *Advances in Confined Detonations and Pulse Detonation Engines*, G. Roy, ed., Torus Press, 2003, pp. 17–40.

[85] R.P. Lindstedt and E.M. Váos, *Transported PDF modeling of high-Reynolds-number premixed turbulent flames*, Combust. Flame 145 (2006), pp. 495–511.

[86] R.P. Lindstedt, H. Ozarovsky, R.S. Barlow, and A.N. Karpetis, *Progression of localized extinction in high Reynolds number turbulent jet flames*, Proc. Combust. Inst. 31 (2007), pp. 1551–1558.

[87] K. Gkagkas and R.P. Lindstedt, *The impact of reduced chemistry on auto-ignition of H_2 in turbulent*

flows, Combust. Theory Model. 13 (2009), pp. 607–64.

[88] B.B.O. Waldheim, *Modelling of soot formation and aromatic growth in laminar flames and reactor systems*, Ph.D. thesis, Imperial College London, 2015.

[89] J.E. de Vries, *Study on turbulent fluctuations in diffusion flames using laser induced fluorescence*, Ph.D. thesis, Delft University of Technology, 1994.

[90] R.W. Bilger, S.H. Stårner, and R.J. Kee, *On reduced mechanisms for methane-air combustion in non-premixed flames*, Combust. Flame 80 (1990), pp. 135–149.

[91] A. Kazakov, H. Wang, and M. Frenklach, *Detailed modeling of soot formation in laminar premixed ethylene flames at a pressure of 10 bar*, Combust. Flame 100 (1995), pp. 111–120.

Appendix A. PAH analogy model for soot surface growth

The soot surface chemistry model by Lindstedt and Louloudi [28, 43] based on naphthalene is shown in Eqs. (I)-(X), and the rate constants are presented in Table A1.

$$\mathrm{C_{10}H_7 + H} \rightleftharpoons \mathrm{C_{10}H_8} \quad \text{(I)}$$
$$\mathrm{C_{10}H_7 + H_2} \rightleftharpoons \mathrm{C_{10}H_8 + H} \quad \text{(II)}$$
$$\mathrm{C_{10}H_8 + O} \rightleftharpoons \mathrm{C_{10}H_7O + H} \quad \text{(III)}$$
$$\mathrm{C_{10}H_8 + OH} \rightleftharpoons \mathrm{C_{10}H_7 + H_2O} \quad \text{(IV)}$$
$$\mathrm{C_{10}H_7 + O_2} \rightleftharpoons \mathrm{C_{10}H_7O + O} \quad \text{(V)}$$
$$\mathrm{C_{10}H_7 + O_2} \rightleftharpoons \mathrm{C_{10}H_7OO} \quad \text{(VI)}$$
$$\mathrm{C_{10}H_7OO} \rightleftharpoons \mathrm{C_9H_7 + CO_2} \quad \text{(VII)}$$
$$\mathrm{C_{10}H_7OO} \rightleftharpoons \mathrm{C_{10}H_6O_2 + H} \quad \text{(VIII)}$$
$$\mathrm{C_{10}H_7O} \rightleftharpoons \mathrm{C_9H_7 + CO} \quad \text{(IX)}$$
$$\mathrm{C_{10}H_7 + C_2H_2} \rightleftharpoons \mathrm{C_{12}H_8 + H} \quad \text{(X)}$$

Reaction (X) corresponds to the soot mass growth step expressed in Eq. (A1).

$$R_G = k_X^f(T)\left[\mathrm{C_{10}H_7}\right]\left[\mathrm{C_2H_2}\right] \quad \text{(A1)}$$

The concentration $\left[\mathrm{C_{10}H_7}\right]$ in Eq. (A1) is obtained via the application of truncated steady-state approximations involving reactions (I)-(X) [43], giving the ratio of concentrations $K_{PAH} = \left[\mathrm{C_{10}H_7}\right]/\left[\mathrm{C_{10}H_8}\right]$ shown in Eq. (A2).

$$K_{PAH} = \frac{K_1K_7 + K_2K_6}{K_4K_7K_9 - K_2K_5K_9 - K_3K_7K_8}K_9 \quad \text{(A2)}$$
$$K_1 = k_I^r + k_{II}^r\left[\mathrm{H}\right] + k_{IV}^f\left[\mathrm{OH}\right] \quad \text{(A3)}$$
$$K_2 = k_V^r\left[\mathrm{O}\right] \quad \text{(A4)}$$
$$K_3 = k_{VI}^r \quad \text{(A5)}$$
$$K_4 = k_I^f\left[\mathrm{H}\right] + k_{II}^f\left[\mathrm{H_2}\right] + k_{IV}^r\left[\mathrm{H_2O}\right] + k_V^f\left[\mathrm{O_2}\right] + k_{VI}^f\left[\mathrm{O_2}\right] + k_X^f\left[\mathrm{C_2H_2}\right] \quad \text{(A6)}$$
$$K_5 = k_V^f\left[\mathrm{O_2}\right] \quad \text{(A7)}$$
$$K_6 = k_{III}^f\left[\mathrm{O}\right] \quad \text{(A8)}$$
$$K_7 = k_{III}^r\left[\mathrm{H}\right] + k_V^r\left[\mathrm{O}\right] + k_{IX}^f \quad \text{(A9)}$$
$$K_8 = k_{VI}^f\left[\mathrm{O_2}\right] \quad \text{(A10)}$$
$$K_9 = k_{VI}^r + k_{VII}^f + k_{VIII}^f \quad \text{(A11)}$$

The emerging naphthalene concentration term is approximated as a function of the maximum number of active sites on the soot surface $\chi_{s-h} \approx 2.32 \times 10^{19}$ sites / ($\mathrm{m^2}$ soot surface) [22, 50] and the soot surface area A_s (via Eq. (56)) as

$$\left[\mathrm{C_{10}H_8}\right] = \alpha_s A_s \frac{\chi_{s-h}}{N_A}\,, \quad \text{(A12)}$$

where $N_A = 6.022 \times 10^{26}\,\mathrm{kmol^{-1}}$ is Avogadro's number and α_s is a modelling parameter expressing the fraction of sites available for reaction, for which a strong sensitivity has been found in previous work [22, 28, 50]. The final expression for growth via the surface

chemistry model is hence given by Eq. (A13).

$$R_G = k_X^f(T)\chi_s A_s \left[C_2H_2\right] \tag{A13}$$

$$\chi_s = K_{PAH}\alpha_s \frac{\chi_{s-h}}{N_A} \tag{A14}$$

Table A1. Reaction rate constants for the PAH analogy of soot surface chemistry [67] presented in the form $A_i\alpha_i T^{\beta_i}\exp(-E_i/RT)$. Units are in K, kmol, m^3 and s.

Step	A_i	α_i	β_i	E_i/R
I	7.83×10^{10}	1	0	0
II	4.44×10^{1}	1	2.43	3,158
III	2.5×10^{10}	1	0	2,347
IV	1.7×10^{5}	1	1.42	729
V	2.15×10^{10}	1	0	3,076
VI	2.5×10^{9}	1	–0.15	80
VII	2.272×10^{8}	1	0	0
VIII	2.272×10^{8}	1	0	0
IX	1.8×10^{11}	1	0	22,062
X	3.57×10^{21}	1	–3.176	7,471

Tables and Figures

Table 2. Governing equations (in order): Reynolds stress closure, turbulent kinetic energy dissipation closure, joint-scalar PDF transport equation, and turbulent transport closure.

$$\frac{\partial \bar{\rho}\widetilde{u_i'' u_j''}}{\partial t} + \frac{\partial \bar{\rho}\widetilde{u_l'' u_i'' u_j''}}{\partial x_l} = T_{ijl} + P_{ij} + \phi_{ij} - \bar{\rho}\delta_{ij}\frac{2}{3}\widetilde{\varepsilon} \tag{15}$$

$$T_{ijl} = \frac{\partial}{\partial x_k}\left[C_s \bar{\rho}\frac{\widetilde{k}}{\widetilde{\varepsilon}}\widetilde{u_k'' u_l''}\frac{\partial \widetilde{u_i'' u_j''}}{\partial x_l}\right] \tag{16}$$

$$P_{ij} = -\bar{\rho}\left[\widetilde{u_i'' u_l''}\frac{\partial \widetilde{u_j}}{\partial x_l} + \widetilde{u_j'' u_l''}\frac{\partial \widetilde{u_i}}{\partial x_l}\right] \tag{17}$$

$$\begin{aligned}\phi_{ij} =& -\left(C_1\widetilde{\varepsilon} + C_1^* P_{kk}\right) b_{ij} + C_2\widetilde{\varepsilon}\left(b_{ik}b_{kj} - \frac{1}{3}b_{mn}b_{mn}\delta_{ij}\right) + \left(C_3 - C_3^*\Pi^{0.5}\right)\widetilde{k}S_{ij} \\ &+ C_4\widetilde{k}\left(b_{ik}S_{jk} + b_{jk}S_{ik} - \frac{2}{3}b_{mn}S_{mn}\delta_{ij}\right) + C_5\widetilde{k}\left(b_{ik}W_{jk} + b_{jk}W_{ik}\right)\end{aligned} \tag{18}$$

$$b_{ij} = \frac{\widetilde{u_i'' u_j''}}{\widetilde{u_k'' u_k''}} - \frac{1}{3}\delta_{ij}, \quad \Pi = b_{ij}b_{ji}, \quad S_{ij} = \frac{1}{2}\left(\frac{\partial \widetilde{u_i}}{\partial x_j} + \frac{\partial \widetilde{u_j}}{\partial x_i}\right), \quad W_{ij} = \frac{1}{2}\left(\frac{\partial \widetilde{u_i}}{\partial x_j} - \frac{\partial \widetilde{u_j}}{\partial x_i}\right) \tag{19}$$

$$C_1 = 3.4, \quad C_1^* = 1.8, \quad C_2 = 4.2, \quad C_3 = 0.8 \tag{20}$$

$$C_3^* = 1.3, \quad C_4 = 1.25, \quad C_5 = 0.40, \quad C_S = 0.22 \tag{21}$$

$$\frac{\partial \bar{\rho}\widetilde{\varepsilon}}{\partial t} + \frac{\partial \bar{\rho}\widetilde{u_l}\widetilde{\varepsilon}}{\partial x_l} = \frac{\partial}{\partial x_k}\left[C_{S\varepsilon}\bar{\rho}\frac{\widetilde{k}}{\widetilde{\varepsilon}}\widetilde{u_k'' u_l''}\frac{\partial \widetilde{\varepsilon}}{\partial x_l}\right] - C_{\varepsilon 1}\frac{\widetilde{\varepsilon}}{\widetilde{k}}P_{kk} - C_{\varepsilon 2}\frac{\widetilde{\varepsilon}}{\widetilde{k}}\widetilde{\varepsilon} \tag{22}$$

$$C_{S\varepsilon} = 0.18, \quad C_{\varepsilon 1} = 1.44, \quad C_{\varepsilon 2} = 1.80 \tag{23}$$

$$\frac{\partial \bar{\rho}\widetilde{f_{\underline{\phi}}}}{\partial t} + \frac{\partial \bar{\rho}\widetilde{u_l}\widetilde{f_{\underline{\phi}}}}{\partial x_l} + \sum_{\alpha=1}^{N}\frac{\partial}{\partial \psi_\alpha}\left[\bar{\rho}S_\alpha\widetilde{f_{\underline{\phi}}}\right] = -\frac{\partial \bar{\rho}\langle u_l''|\underline{\psi}\rangle\widetilde{f_{\underline{\phi}}}}{\partial x_l} + \sum_{\alpha=1}^{N}\frac{\partial}{\partial \psi_\alpha}\left[\left\langle\frac{1}{\rho}\frac{\partial}{\partial x_l}J_{l,\alpha}\middle|\underline{\psi}\right\rangle\bar{\rho}\widetilde{f_{\underline{\phi}}}\right] \tag{24}$$

$$-\frac{\partial \bar{\rho}\langle u''|\underline{\psi}\rangle\widetilde{f_{\underline{\phi}}}}{\partial x_l} = -\frac{\partial}{\partial x_l}\left(\frac{\mu_t}{\sigma_t}\frac{\partial \widetilde{f_{\underline{\phi}}}}{\partial x_l}\right) \tag{25}$$

Table 3. Composition of Delft flame main fuel jet in percent mole fraction in experiments and model: Dutch natural gas, Californian natural gas diluted with N_2, Adelaide natural gas diluted with N_2, and modified compositions of the latter two (Model 1 and 2).

Component	Dutch [31, 89]	Californian [33]	Model 1	Adelaide [34]	Model 2
CH_4	81.29	81.70	81.70	79.89	79.89
C_2H_6	2.87	3.00	3.10	3.72	3.92
C_nH_m	0.62	0.10	0.00	0.20	0.00
N_2	14.32	14.60	14.60	13.97	13.97
O_2	0.01	0.00	0.00	0.00	0.00
CO_2	0.89	0.60	0.60	2.22	2.22

Table 4. Reaction rate constants for soot nucleation via Eq. (49) presented in the form $k_{N,i} = A_i \exp(-E_i/RT)$. Units are in K, kmol, m^3 and s.

k_i	A_i	α_i	β_i	E_i/R	Source
$k_{N,1}$	6.30×10^3	1	0	21,000	Lindstedt [22]
$k_{N,2}$	3.79×10^1	1	0	17,500	Sunderland and Faeth [59]
$k_{N,3}$	6.30×10^1	1	0	21,000	Current work
$k_{N,4}$	3.78×10^1	1	0	21,000	Current work
$k_{N,5}$	1.89×10^1	1	0	21,000	Current work
$k_{N,6}$	9.45	1	0	21,000	Current work

Table 5. Reaction rate constants for soot growth and oxidation in Eqs. (54) and (59)-(61) presented in the form $A_i \alpha_i T^{\beta_i} \exp(-E_i/RT)$ [22, 43, 82]. Units are in K, kmol, m^3 and s.

k_i	A_i	α_i	β_i	E_i/R
k_G	7.50×10^2	1	0	12,100
k_O	9.09	0.20	1/2	0
$k_{OH,1}$	8.82	0.05	1/2	0
$k_{O_2,1}$	6.43	0.723	1/2	11,250
$k_{OH,2}$	8.82	0.10	1/2	0
$k_{O_2,2}$	6.43	116	1/2	19,680

Table 6. Modes of the measured and calculated PSDs in the WSR and at Ports 1 and 3 of the WSR/PFR configuration of Manzello et al. [8]. Measurements by Lenhert and Manzello [9]. Units in nm.

	WSR	PFR Port 1	PFR Port 3
Measurements	4.2	7.6	7.7
A_4 nucleation	4.8	6.2	8.2
C_2H_2 nucleation, $k_{N,1}$	9.4	14.1	21.1
C_2H_2 nucleation, $k_{N,2}$	5.5	8.2	10.7
C_2H_2 nucleation, $k_{N,3}$	4.8	6.2	7.1
C_2H_2 nucleation, $k_{N,4}$	4.8	5.5	7.1
C_2H_2 nucleation, $k_{N,5}$	4.8	5.5	6.2
C_2H_2 nucleation, $k_{N,6}$	4.8	4.8	5.5

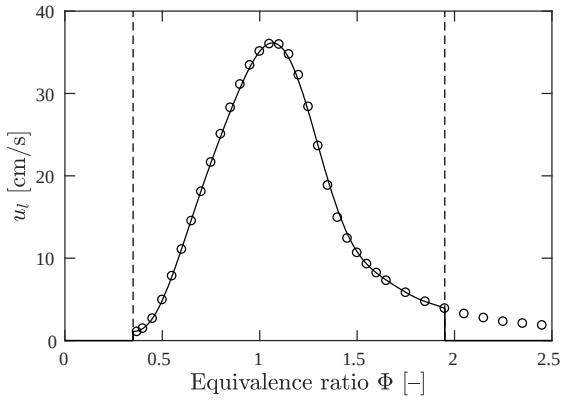

Figure 1. Laminar burning velocity of natural gas obtained from laminar premixed flame calculations with strain rate $a \approx 100$ s^{-1} (○) with a sum-of-sines fit for $0.35 \leq \Phi \leq 1.95$ (—).

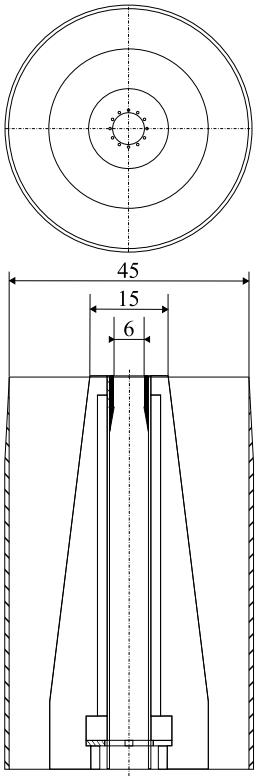

Figure 2. Top and side view of the Delft burner head. Measurements in mm.

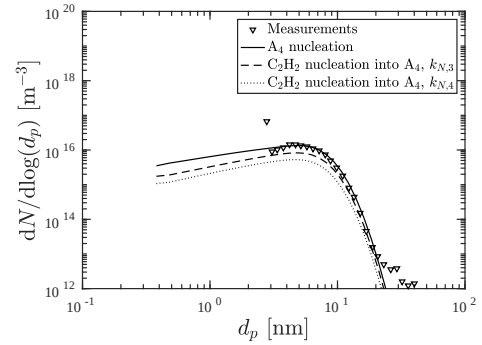

(a) WSR

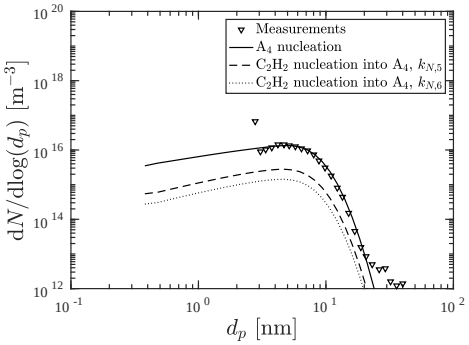

(b) WSR

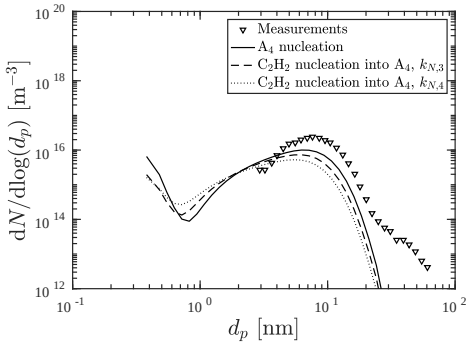

(c) PFR Port 1

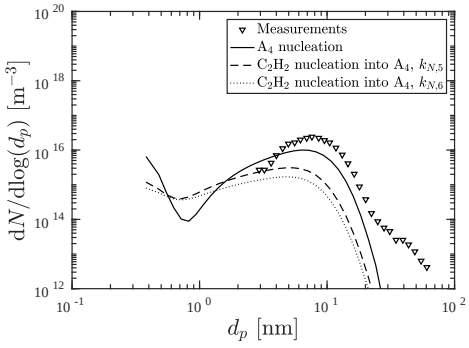

(d) PFR Port 1

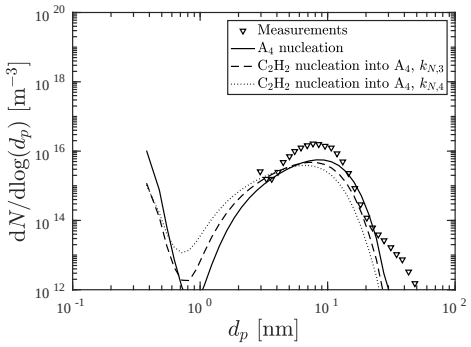

(e) PFR Port 3

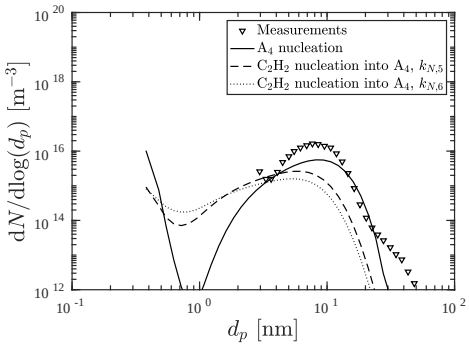

(f) PFR Port 3

Figure 3. Calculated soot particle size distributions in the WSR and at PFR Ports 1 and 3 of the WSR/PFR setup of Lenhert and Manzello [9] with C_2H_4air at $\Phi = 2.0$ and $T_{WSR} = 1723$ K. Comparison of measurements and computations using pyrene (A_4) and acetylene based nucleation models with reaction rate coefficients $k_{N,3}$, $k_{N,4}$, $k_{N,5}$ and $k_{N,6}$ from Table 4. The updated oxidation rates $k_{OH,2}$ and $k_{O_2,2}$ were used.

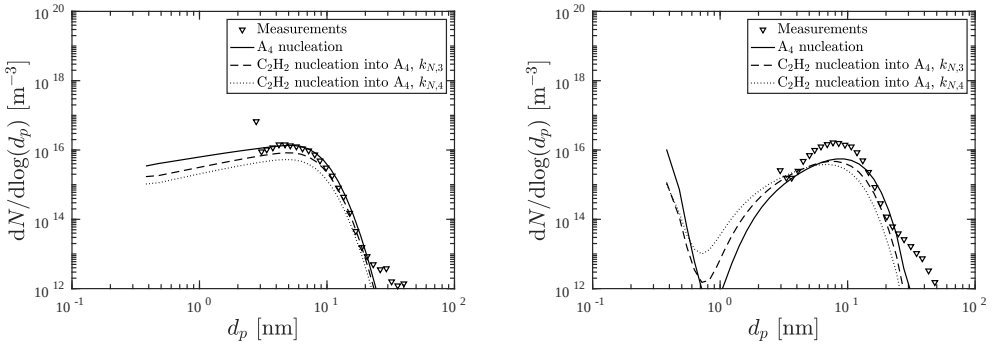

(a) WSR (b) PFR Port 3

Figure 4. Calculated soot particle size distributions in the WSR and at PFR Port 3 of the WSR/PFR setup of Lenhert and Manzello [9] with C_2H_4/air at $\Phi = 2.0$ and $T_{WSR} = 1723$ K. Comparison of measurements and computations using pyrene (A_4) and acetylene based nucleation models with reaction rate coefficients $k_{N,3}$ and $k_{N,4}$ from Table 4. The oxidation rates $k_{OH,1}$ and $k_{O_2,1}$ were used.

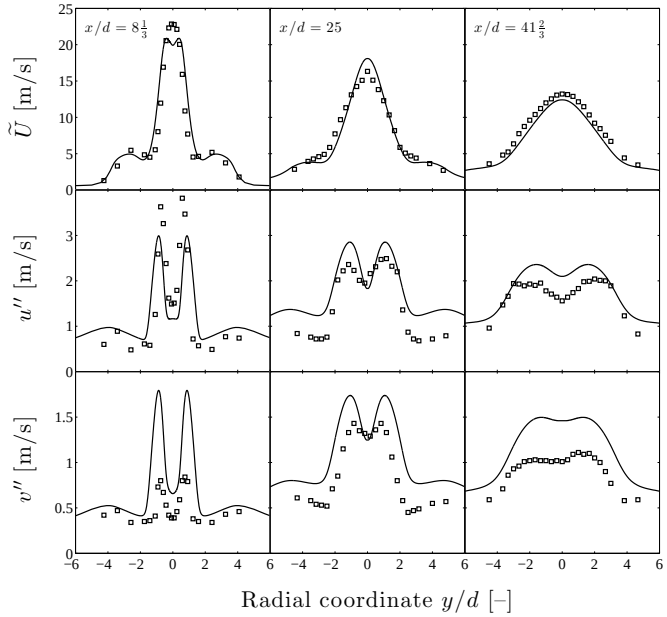

Figure 5. Radial profiles of Favre mean axial velocity $\widetilde{U}$ and RMS of axial (u'') and radial (v'') velocity in the Delft III / Adelaide flame at axial positions $8\frac{1}{3} \leq x/d \leq 41\frac{2}{3}$. Comparison of calculations (lines) to experimental data (symbols) by Stroomer [31]. The fuel composition is "Model 1" defined in Table 3.

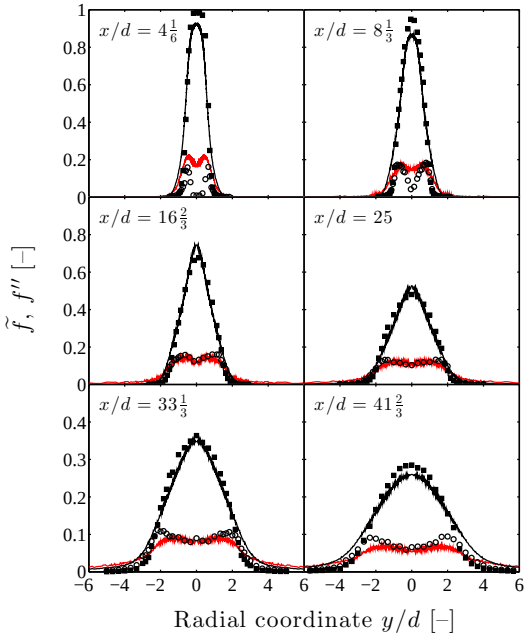

Figure 6. Calculated radial profiles of Favre mean mixture fraction ($\widetilde{f}$, black lines) and its RMS (f'', red lines) in the Delft III / Adelaide flame at axial positions $8\frac{1}{3} \leq x/d \leq 41\frac{2}{3}$. Comparison to mean (closed symbols) and RMS (open symbols) from experimental data by Nooren et al. [32, 33]. The fuel composition is "Model 1" defined in Table 3.

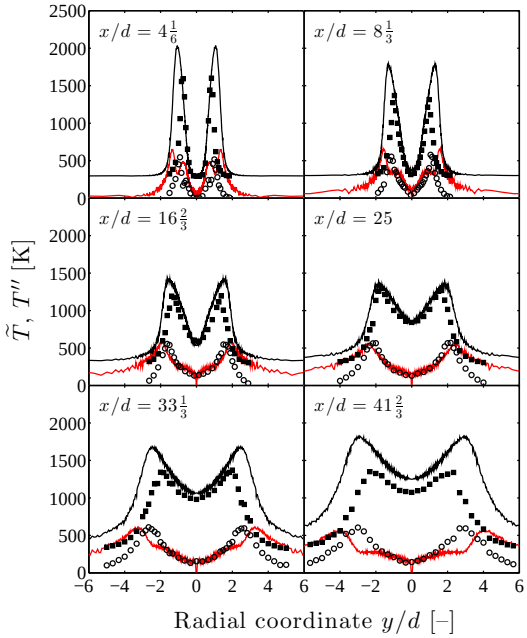

Figure 7. Calculated radial profiles of Favre mean temperature ($\widetilde{T}$, black lines) and its RMS (T'', red lines) in the Delft III / Adelaide flame at axial positions $8\frac{1}{3} \leq x/d \leq 41\frac{2}{3}$. Comparison to mean (closed symbols) and RMS (open symbols) from experimental data by Nooren et al. [32, 33]. The fuel composition is "Model 1" defined in Table 3.

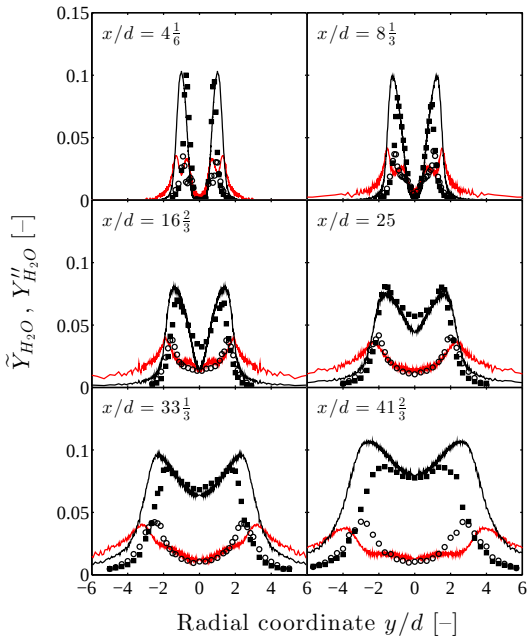

Figure 8. Calculated radial profiles of Favre mean H_2O mass fraction ($\widetilde{y}_{H_2O}$, black lines) and its RMS (y''_{H_2O}, red lines) in the Delft III / Adelaide flame at axial positions $8\frac{1}{3} \leq x/d \leq 41\frac{2}{3}$. Comparison to mean (closed symbols) and RMS (open symbols) from experimental data by Nooren et al. [32, 33]. The fuel composition is "Model 1" defined in Table 3.

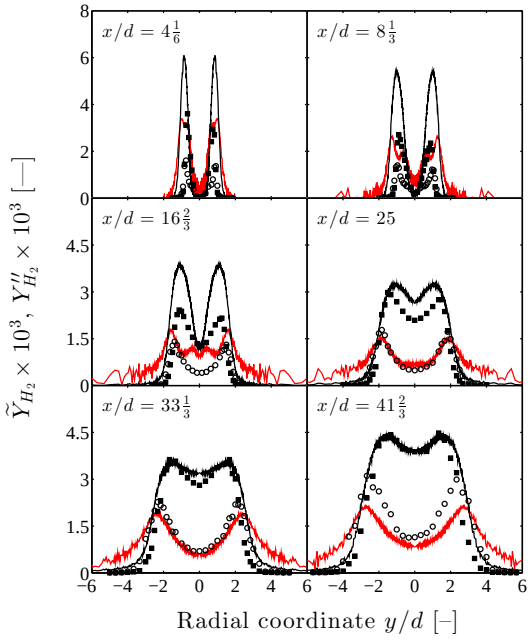

Figure 9. Calculated radial profiles of Favre mean H_2 mass fraction ($\widetilde{y}_{H_2}$, black lines) and its RMS (y''_{H_2}, red lines) in the Delft III / Adelaide flame at axial positions $8\frac{1}{3} \leq x/d \leq 41\frac{2}{3}$. Comparison to mean (closed symbols) and RMS (open symbols) from experimental data by Nooren et al. [32, 33]. The fuel composition is "Model 1" defined in Table 3.

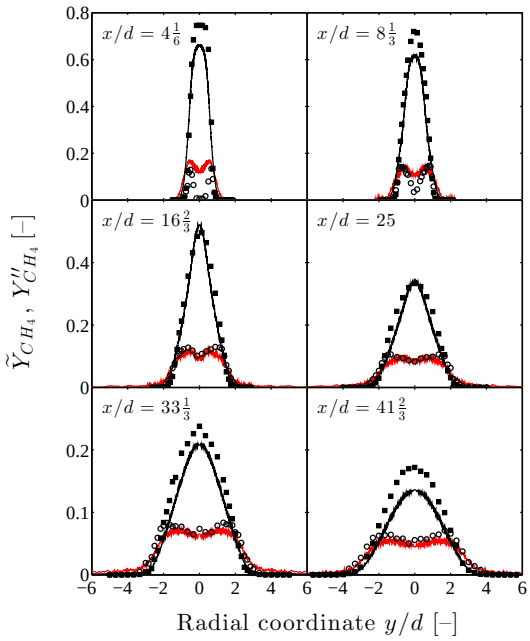

Figure 10. Calculated radial profiles of Favre mean CH_4 mass fraction ($\widetilde{y}_{CH_4}$, black lines) and its RMS (y''_{CH4}, red lines) in the Delft III / Adelaide flame at axial positions $8\frac{1}{3} \leq x/d \leq 41\frac{2}{3}$. Comparison to mean (closed symbols) and RMS (open symbols) from experimental data by Nooren et al. [32, 33]. The fuel composition is "Model 1" defined in Table 3.

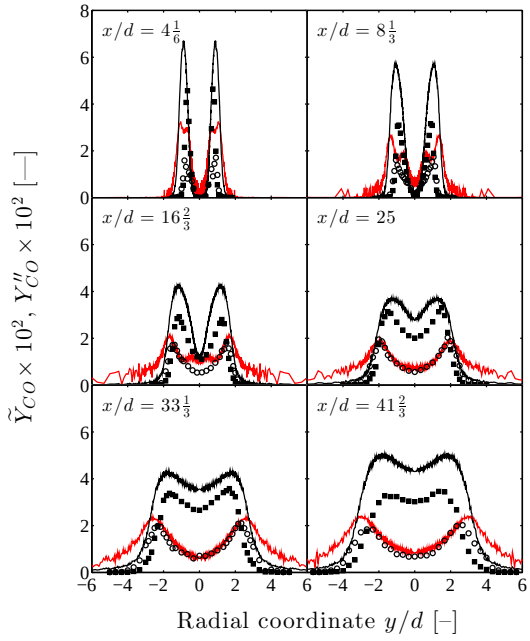

Figure 11. Calculated radial profiles of Favre mean CO mass fraction ($\widetilde{y}_{CO}$, black lines) and its RMS (y''_{CO}, red lines) in the Delft III / Adelaide flame at axial positions $8\frac{1}{3} \leq x/d \leq 41\frac{2}{3}$. Comparison to mean (closed symbols) and RMS (open symbols) from experimental data by Nooren et al. [32, 33]. The fuel composition is "Model 1" defined in Table 3.

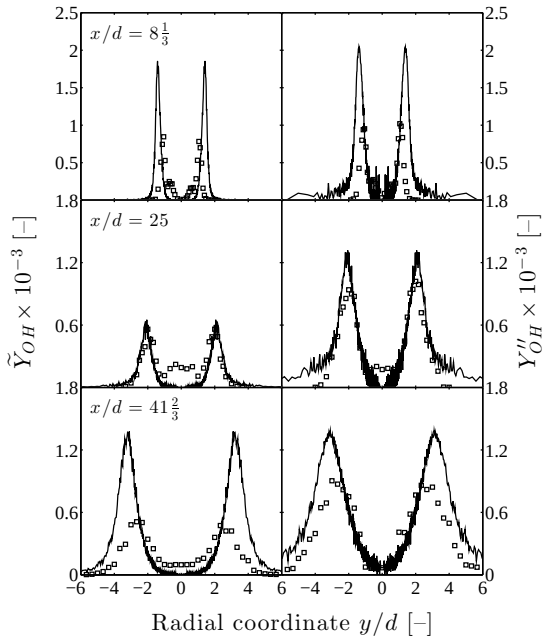

Figure 12. Radial profiles of Favre mean OH mass fraction ($\widetilde{y}_{OH}$, left) and its RMS (y''_{OH}, right) in the Delft III / Adelaide flame at axial positions $8\frac{1}{3} \leq x/d \leq 41\frac{2}{3}$. Comparison of calculations (lines) to experimental data (symbols) by Nooren et al. [32, 33]. The fuel composition is "Model 1" defined in Table 3.

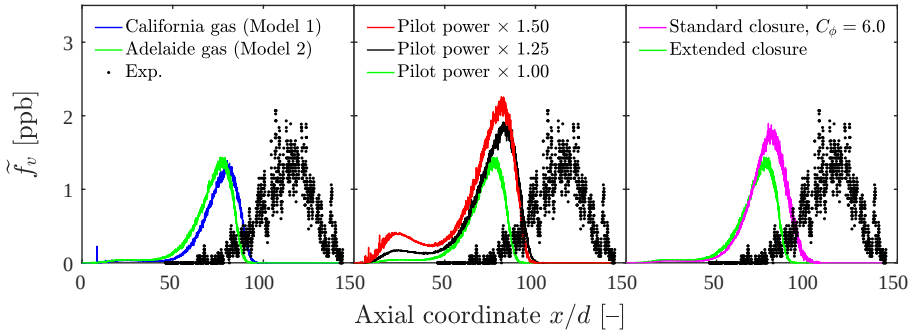

Figure 13. Centreline profiles of Favre mean of soot volume fraction in the Delft III / Adelaide flame, showing the influence of the gas composition (left), the increase in thermal power of the pilot model compared to the experimental value of 196 W (center), and the scalar dissipation rate closure (right). The two-equation model including the PAH analogy model for soot surface chemistry with $\alpha_s = 0.85$ and rates $k_{N,6}$, $k_{OH,2}$, $k_{O_2,2}$ is used. Comparison to experimental data ($\bullet$) by Qamar et al. [34].

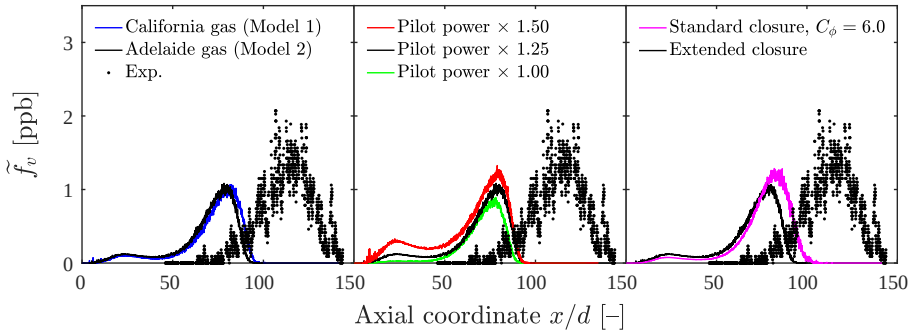

Figure 14. Centreline profiles of Favre mean of soot volume fraction in the Delft III / Adelaide flame, showing the influence of the gas composition (left), the increase in thermal power of the pilot model compared to the experimental value of 196 W (center), and the scalar dissipation rate closure (right). The two-equation model including the PAH analogy model for soot surface chemistry with $\alpha_s = 0.50$ and rates $k_{N,4}$, $k_{OH,2}$, $k_{O_2,2}$ is used. Comparison to experimental data ($\bullet$) by Qamar et al. [34].

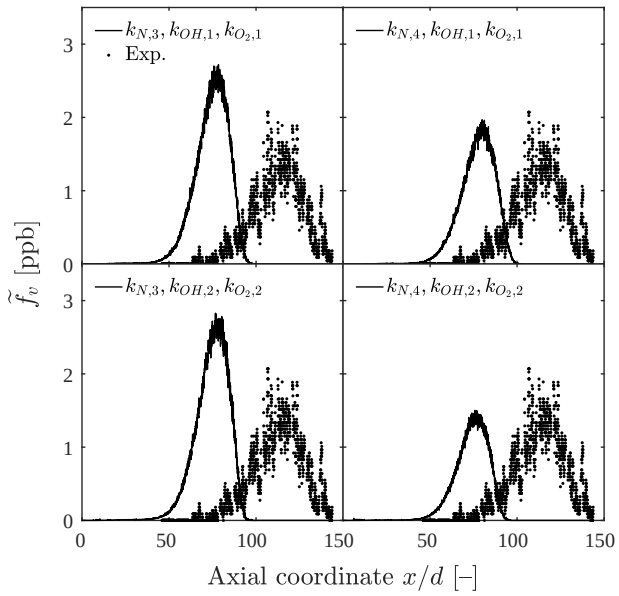

Figure 15. Centreline profiles of Favre mean of soot volume fraction in the Delft III / Adelaide flame. Comparison of predictions (—) from the two-equation model to experimental data (•) by Qamar et al. [34]. The fuel composition is "Model 2" defined in Table 3, α_s = 0.50 and the pilot power 245 W.

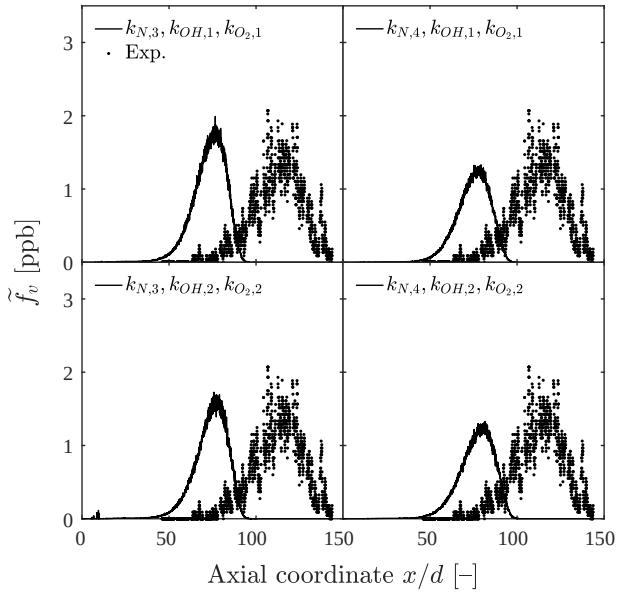

Figure 16. Centreline profiles of Favre mean of soot volume fraction in the Delft III / Adelaide flame. Comparison of predictions (—) from the method of moments model with M_0–M_3 included to experimental data (•) by Qamar et al. [34]. The fuel composition is "Model 2" defined in Table 3, α_s = 0.50 and the pilot power 245 W.

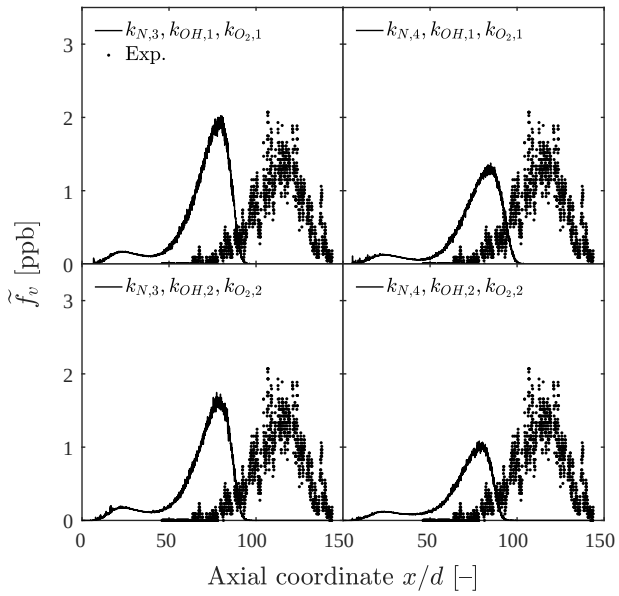

Figure 17. Centreline profiles of Favre mean of soot volume fraction in the Delft III / Adelaide flame. Predictions (—) from the two-equation model including the PAH analogy model for soot surface chemistry with α_s = 0.50. Comparison to experimental data ($\bullet$) by Qamar et al. [34]. The fuel composition is "Model 2" defined in Table 3, α_s = 0.50 and the pilot power 245 W.

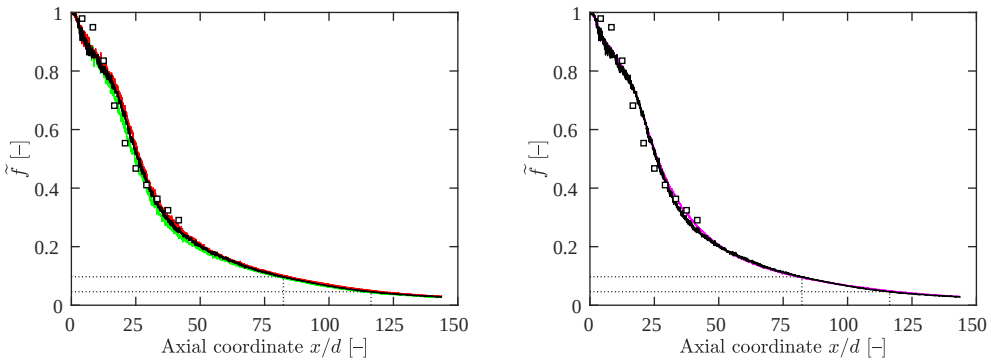

(a) (b)

Figure 18. Centreline profiles of calculated Favre mean mixture fraction in the Delft III / Adelaide flame, illustrating the influence of (a) the pilot source term and (b) the scalar time-scale closure. Results calculated using the extended time-scale closure with a pilot source term corresponding to 1 (green line), 1.25 (black lines) and 1.5 (red line) times the experimental pilot power (196 W) are shown, as well as predictions using a pilot source term of 245 W the standard time-scale closure and C_ϕ = 6.0 (magenta line). Soot peak locations from the calculations shown in black at $x/d \approx 82$ and measurements at $x/d \approx 116$ and the corresponding calculated mixture fraction are shown as ($\cdots$). Comparison to experimental data (□) by Nooren et al. [32, 33]. The fuel composition is "Model 1" defined in Table 3.

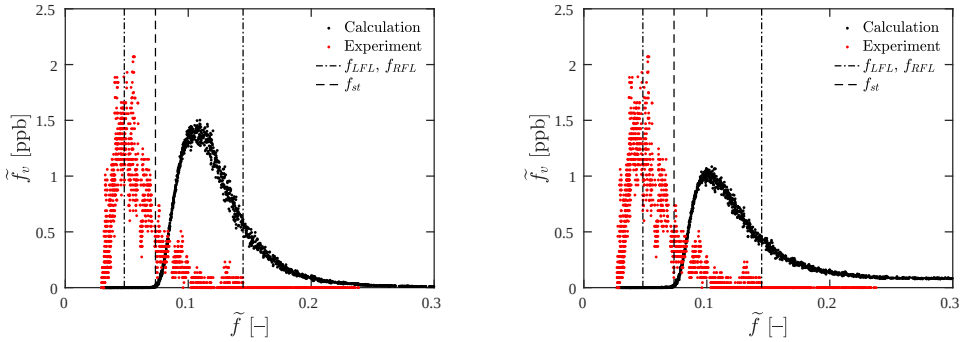

(a) (b)

Figure 19. Favre mean soot volume fraction at the centreline in mixture fraction space in the Delft III / Adelaide flame. Predictions from the two-equation model with $k_{N,4}, k_O, k_{OH,2}, k_{O_2,2}$. (a) The standard growth step and (b) the PAH analogy for soot surface chemistry were used. Comparison to experimental data by Qamar et al. [34], where the mapping to mixture fraction was obtained from the respective calculations. The lean and rich flammability limits of methane f_{LFL}, f_{RFL} and the stoichiometric mixture fraction for the Adelaide natural gas f_{st} are shown for comparison. The fuel composition is "Model 2" defined in Table 3..

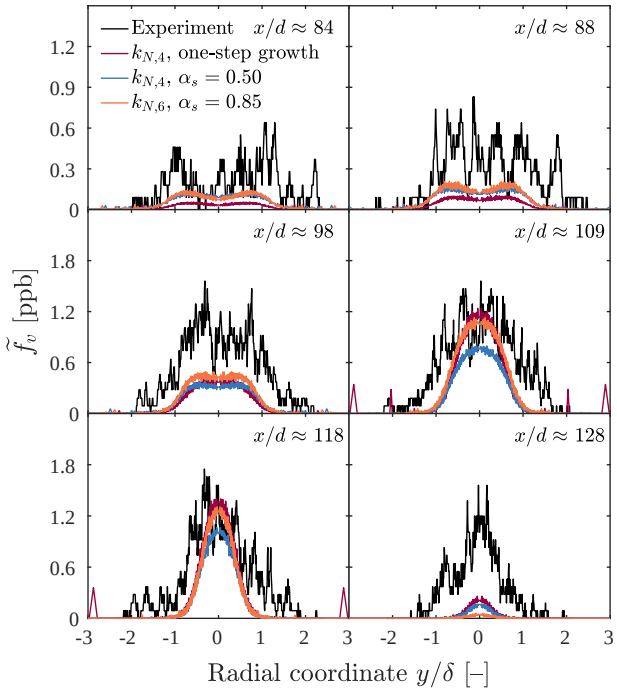

Figure 20. Radial profiles of Favre mean of soot volume fraction in the Delft flame. Comparison of computations featuring the two-equation model with experimental data (black lines) by Qamar et al. [34]. The oxidation rates $k_{OH,2}, k_{O_2,2}$ are used for calculations. Results for $k_{N,4}$ and one-step soot growth (red lines), $k_{N,4}$ and the PAH analogy to surface growth with $\alpha_s = 0.50$ (blue lines) or $k_{N,6}$ with PAH growth and $\alpha_s = 0.85$ (orange lines) are shown. A pilot power of 245 W for the two former calculations and 196 W for the latter is used. The axial locations of the measured profiles are shown with the radial locations normalised to account for the rate of spread of the jet. The fuel composition is "Model 2" defined in Table 3.